



# SUMMER INTERN PROGRAM IN PLANETARY SCIENCE

Papers Presented at the

**26** th  
annual

August 13, 2010 — Houston, Texas

*Papers Presented at the*

# **Twenty-Sixth Annual Summer Intern Conference**

*August 12, 2010  
Houston, Texas*

2010 Summer Intern Program for Undergraduates  
Lunar and Planetary Institute

Sponsored by  
Lunar and Planetary Institute  
NASA Johnson Space Center



Compiled in 2010 by

Meeting and Publication Services  
Lunar and Planetary Institute  
USRA Houston

3600 Bay Area Boulevard, Houston TX 77058-1113

The Lunar and Planetary Institute is operated by the Universities Space Research Association under a cooperative agreement with the Science Mission Directorate of the National Aeronautics and Space Administration.

Any opinions, findings, and conclusions or recommendations expressed in this volume are those of the author(s) and do not necessarily reflect the views of the National Aeronautics and Space Administration.

Material in this volume may be copied without restraint for library, abstract service, education, or personal research purposes; however, republication of any paper or portion thereof requires the written permission of the authors as well as the appropriate acknowledgment of this publication.

## HIGHLIGHTS

---

### Special Activities

June 7, 2010	Tour of the Lunar Curatorial Facility	JSC
June 7, 2010	Tour of the Stardust Laboratory	JSC
June 29, 2010	Tour of the Antarctic Meteorite Laboratory	JSC
August 4, 2010	Robonaut 2 (R2) <i>Attended the Historic First Crew Departure Event for a Humanoid Robot Head to Space</i>	JSC

### Intern Brown Bag Seminars

<i>Date</i>	<i>Speaker</i>	<i>Topic</i>	<i>Location</i>
June 16, 2010	Allan Treiman	Rocks from Mars	LPI
June 23, 2010	Carlton Allen	Astrobiology	JSC
June 30, 2010	David Mittlefehldt	Vesta and the Dawn Mission	JSC
July 7, 2010	Walter Kiefer	Venus	LPI
<b>July 14, 2010</b>	<b>Interns</b>	<b>Intern Mid-Term Reports</b>	<b>LPI</b>
July 21, 2010	Pat McGovern	Mars	LPI
July 28, 2010	Dean Eppler	Apollo Explores the Moon	JSC
August 4, 2010	Paul Spudis	Future of the space program	LPI
August 5, 2010	Don Pettit	Basic Astronautics	JSC
August 11, 2010	Paul Schenk	Satellites of the Giant Planets	LPI



## AGENDA

---

- 8:30 a.m. Breakfast
- 8:45 a.m. Introductory Remarks by Dr. Paul Spudis, Chair and Staff Scientist
- 9:00 a.m. **ANNIE WINTZER, University of Florida**  
(Advisors: C. C. Allen and D. Z. Oehler)  
*Phyllosilicate Deposits in Shalbatana Vallis*
- 9:20 a.m. **AARON BAUER, Williams College** (Advisor: T. F. Stepinski)  
*Automatic Identification of Lunar Craters from Global Topography*
- 9:40 a.m. **TIFFANY ENGLE, Sam Houston State University**  
(Advisors: A. H. Treiman and J. Gross)  
*Mineral Chemistry and Origin of Spinel Bearing Rocks in Lunar Highland Meteorites*
- 10:00 a.m. **JOEL HECKER, University of Cincinnati**  
(Advisor: P. D. Spudis)  
*Properties of Lunar Polar Deposits Revealed by the Mini-RF Imaging Radar on the Chandrayaan-1 and Lunar Reconnaissance Orbiter Missions*
- 10:20 a.m. BREAK
- 10:40 a.m. **ABIGAIL KOSS, Massachusetts Institute of Technology**  
(Advisors: B. Sutter and D. Ming)  
*Interaction of Calcite and SO<sub>2</sub> in Mars Phoenix Thermal and Evolved-Gas Analyzer*
- 11:00 a.m. **ADAM KOSTER, Calvin College**  
(Advisor: D. C. Golden)  
*Experimental Weathering of Olivine, Mg-Siderite, and Olivine-Basalt with Sulfuric Acid: Implications for the Formation of Hematite-Associated Sediments in Meridiani Planum, Mars*
- 11:20 a.m. **CAMERON MERCER, Middlebury College**  
(Advisors: J. H. Jones and D. S. Draper)  
*Experimental Evolution of Yamato 980459 via Equilibrium Crystallization at 0.5 GPa: Approaching Queen Alexandra Range 94201?*
- 11:40 a.m. LUNCH
- 12:30 p.m. **SEAN MURPHY, Lafayette College**  
(Advisor: P. M. Schenk)  
*In Search of Rayed Impact Craters for Insight into the Recent History of Saturn's Icy Moons*
- 12:50 p.m. **WILLIAM VAUGHAN, University of Chicago**  
(Advisors: A. Wittmann and K. H. Joy)  
*Impact Melts and Granulites in the Lunar Meteorite PCA 02007*

- 1:10 p.m. **KATELYN VERNER, Southern Methodist University**  
(Advisors: P. J. McGovern and G. A. Galgana)  
*New Insights into the Structure and Evolution of Large Volcanoes on Venus from High-Resolution Stereo-Derived Topography*
- 1:30 p.m. **KATHRYN VOLK, Northern Illinois University**  
(Advisors: P. B. Niles and R. A. Socki)  
*Covariant C and O Isotope Trends in Some Terrestrial Carbonates and ALH 84001: Possible Linkage Through Similar Formation Processes*
- 1:50 p.m. ADJOURN

## CONTENTS

---

Automatic Identification of Lunar Craters from Global Topography <i>A. W. Bauer and T. F. Stepinski</i> .....	1
Mineral Chemistry and Origin of Spinel Bearing Rocks in Lunar Highland Meteorites <i>T. R. Engle, J. Gross, and A. H. Treiman</i> .....	4
Properties of Lunar Polar Deposits Revealed by the Mini-RF Imaging Radar on the Chandrayaan-1 and Lunar Reconnaissance Orbiter Missions <i>J. W. Hecker and P. D. Spudis</i> .....	7
Investigation of Orthopyroxene Diversity in Howardite Meteorites <i>K. N. Johnson, D. W. Mittlefehldt, and J. S. Herrin</i> .....	10
Interaction of Calcite and SO <sub>2</sub> in Mars Phoenix Thermal and Evolved-Gas Analyzer <i>A. R. Koss and B. Sutter</i> .....	13
Experimental Weathering of Olivine, Mg-Siderite, and Olivine-Basalt with Sulfuric Acid: Implications for the Formation of Hematite-Associated Sediments in Meridiani Planum, Mars. <i>A. M. Koster and D. C. Golden</i> .....	16
Experimental Evolution of Yamato 980459 via Equilibrium Crystallization at 0.5 GPa: Approaching Queen Alexandra Range 94201? <i>C. M. Mercer, J. H. Jones, D. S. Draper, T. Usui, and L. H. Le</i> .....	19
In Search of Rayed Impact Craters for Insight into the Recent History of Saturn's Icy Moons <i>S. W. Murphy and P. M. Schenk</i> .....	22
Impact Melts and Granulites in the Lunar Meteorite PCA 02007 <i>W. M. Vaughan, A. Wittmann, K. H. Joy, and D. A. Kring</i> .....	25
New Insights into the Structure and Evolution of Large Volcanoes on Venus from High-Resolution Stereo-Derived Topography <i>K. R. Verner, G. A. Galgana, and P. J. McGovern</i> .....	28
Covariant C and O Isotope Trends in Some Terrestrial Carbonates and ALH 84001: Possible Linkage through Similar Formation Processes <i>K. E. Volk, P. B. Niles, and R. A. Socki</i> .....	31
Phyllosilicate Deposits in Shalbatana Vallis <i>A. E. Wintzer, C. C. Allen, and D. Z. Oehler</i> .....	34



**AUTOMATIC IDENTIFICATION OF LUNAR CRATERS FROM GLOBAL TOPOGRAPHY.** A. W. Bauer<sup>1</sup> and T. F. Stepinski<sup>2</sup>, <sup>1</sup>Williams College, Williamstown, MA 01267 (awb1@williams.edu), <sup>2</sup>Lunar and Planetary Institute, Houston, TX 77058 (tstepinski@lpi.usra.edu).

**Introduction:** Impact craters are a vital tool in understanding the history of planetary surfaces. As structures resulting from the collision of meteoroids with planetary surfaces, an analysis of their characteristics, including depth-to-diameter ratio, can yield insights into many geomorphologic processes. Furthermore, examining the density of craters on a given surface is the primary method of estimating the age of a planetary surface. A catalog of impact craters is useful in facilitating these analyses by providing a single, standardized repository for crater locations and attributes. The best currently available catalog of lunar craters [1] lists the locations and diameters (but not depths) of 8497 craters. This represents only a small portion of the total number of lunar craters and is insufficient for comprehensive global analysis.

A new global, 64 pixels/degree digital elevation model (DEM) of the Moon [2] based on altimetry measurements provided by the Lunar Orbiter Laser Altimeter (LOLA) instrument aboard the Lunar Reconnaissance Orbiter (LRO) gives an opportunity to generate a more extensive lunar crater catalog. Craters having diameters  $> 3$  km are recognizable in the DEM and we should be able to identify them through an automated procedure that employs a crater detection computer algorithm. The ultimate goal of this study is to catalog all craters present in the DEM; we estimate that, when

finished, our catalog will list positions, diameters and depths of more than 20,000 craters. A significant benefit of working with the DEM instead of an image is the ability to estimate depth of each crater. This will allow for global depth-to-diameter ratio maps to be constructed.

**Methods:** The computer algorithm we are using to generate the catalog of lunar craters is based on methods described by Stepinski et al. [3] in the context of Martian craters. The algorithm has two major components: a topographic depression-finding algorithm called Cratermatic [4] that searches the entire surface for locations that have the potential to be craters (crater candidates) and a machine-learning-based classifier that makes a final decision whether a candidate is a crater or not. Because of computer memory limitation our algorithm cannot be applied to the entire lunar surface, so instead the global DEM is divided into numerous overlapping square tiles. 108 equatorial tiles are shown in Figure 1; in addition there are 56 polar tiles not shown here. The algorithm is applied to each tile separately and the results are combined to yield the global catalog. Each equatorial tile is 24 degrees on a side and overlaps with each of its neighbors by four degrees. The tiles overlap to accommodate craters that may be located on the edge of a tile.

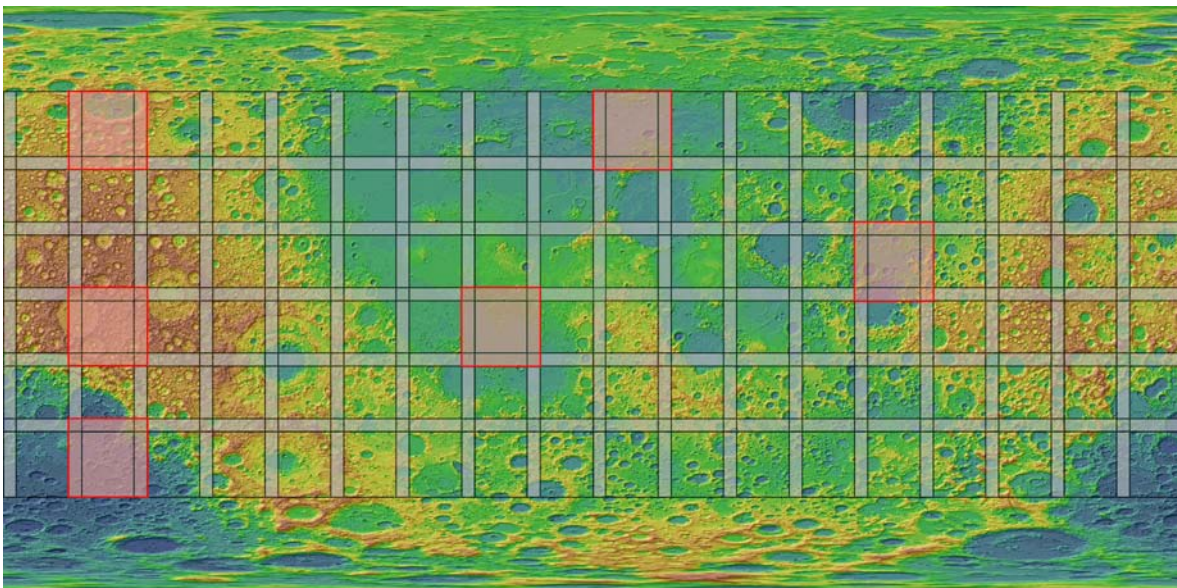


**Figure 1.** The tiling scheme for the equatorial region of the lunar DEM. The polar regions are tiled separately. The gray areas show the overlap between tiles. The areas highlighted in red are the locations of our ground truth set.

*Depression-finding algorithm.* The Cratermatic algorithm operates on topographic data and calculates the location and extent of all the depressions present in the data. If the algorithm attempted to find all depressions simultaneously, it would have no way of detecting nested depressions, which are common to cratered surfaces including the Moon. To avoid this problem, the algorithm only finds depressions of approximately radius  $r$  at any one time, beginning with the smallest depressions and ending with the largest. The final step of the Cratermatic algorithm is to characterize each candidate and perform preliminary elimination of candidates that are obviously not craters. Elimination is based upon a collection of calculated parameters that describe the crater candidate's shape. A threshold is chosen for each parameter and any potential crater which has at least one parameter that exceeds the corresponding threshold is not included in the final set of crater candidates. It was necessary to empirically fine-tune these threshold values to suit the lunar environment. Doing so avoids eliminating actual craters from the pool of candidates. The final output of Cratermatic for a portion of one tile is shown in Figure 2.

*Machine-learning algorithm.* The preliminary elimination of candidates by Cratermatic algorithm is performed using set of hand-made evaluation rules. No such set of rules is comprehensive enough to accurately differentiate between craters and non-craters in the pool of candidates. A more accurate separation can be achieved by means of supervised classification. Each candidate is represented as a vector of five features:  $\{D, d, d/D, m_2, m_3\}$ .  $D$  is the candidate's diameter,  $d$  is its depth, and  $m_2$  and  $m_3$  are calculated values representing the elongation and lumpiness, respectively, of the candidate's shape. In supervised learning a supervisor (human being) labels as craters and non-craters a representative number of candidates. Using these labels and the features of the labeled candidates the machine learning algorithm yields a classifier – a function that when presented with an unlabeled candidate will predict whether it's a crater or not.

**Results:** The ultimate goal of this project is to obtain a global catalog of all lunar craters present in the 64 pixels/degree DEM. During the limited time of this internship we have identified crater candidates in all tiles (equatorial and polar). In each tile we divided the candidates into three categories based on how they are generated by the Cratermatic algorithm. Basically, the first category contains the smallest candidates, the second category contains the medium candidates, and the third category contains the largest candidates. Because crater characteristics are size-dependent, a sepa-

rate classifier needs to be constructed for each category. We focused on finding the best classifier for the first category of craters.

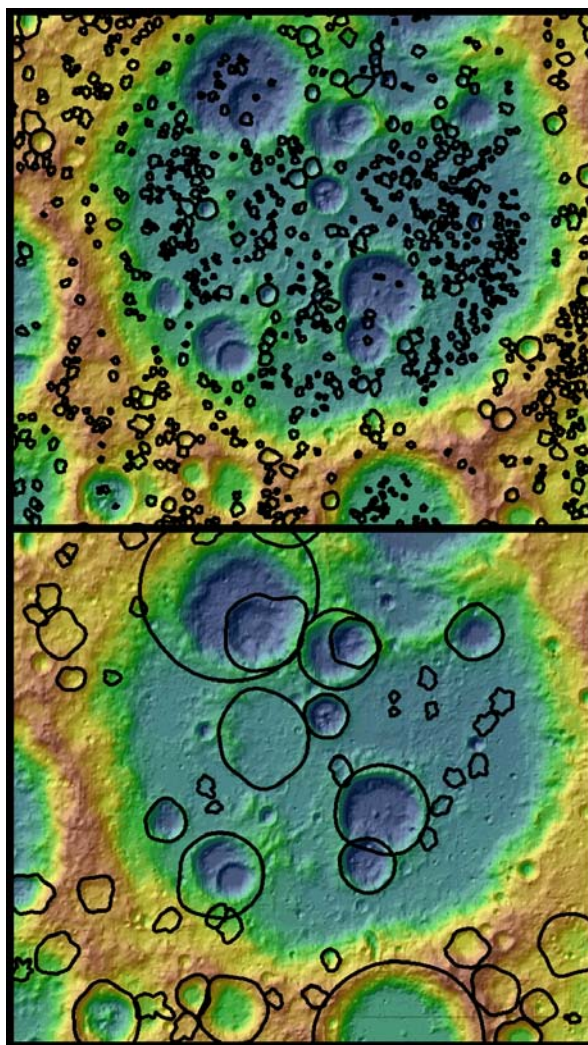


**Figure 2.** The results of the depression-detection algorithm for a portion of one tile. The top image shows the results for the two smallest radii increments and the bottom image shows the results for the remaining radii.

In order to test the performance of various classifiers we have established a “ground truth set” of candidates. These are candidates which have been manually labeled. Six morphologically different terrain types were selected from six different equatorial tiles (highlighted in red in Figure 1) for exhaustive labeling. In total we have labeled 2561 candidates; 1271 of them were labeled as craters and the remaining 1290 as non craters. Using this ground truth we experimented with different machine-learning algorithms to establish which is most appropriate for our task. Table 1 summarizes the results.

		Boosted?	Average accuracy	Average TPR	Average FPR
Merging	C4.5	Yes	0.712	0.935	0.473
		No	0.799	0.884	0.273
	SMO	Yes	0.661	0.920	0.575
		No	0.661	0.920	0.575
	RandomForest	Yes	0.705	0.953	0.517
		No	0.705	0.953	0.517
Single	C4.5	Yes	0.673	0.618	0.265
		No	0.676	0.623	0.263
	SMO	Yes	0.682	0.551	0.190
		No	0.682	0.551	0.190
	RandomForest	Yes	0.661	0.619	0.297
		No	0.669	0.636	0.297

**Table 1.** The results of our machine-learning classifier analysis. Our testing protocols are described below. The accuracy is the proportion of correctly identified craters, the TPR (truth positive rate) is the proportion of actual craters that were correctly identified, and the FPR (false positive rate) is the proportion of actual non-craters that were incorrectly identified as craters.

We used the three different machine-learning algorithms: the C4.5 decision tree algorithm [5], the Random Forest algorithm [6], and the SMO algorithm [7] as implemented by the WEKA machine-learning software [8]. Two testing protocols were performed; both are based on the idea of cross validation. In cross validation we use training samples from five out of six terrains and test on the remaining terrain. This is repeated for all six terrains and the average results are reported. In the first protocol (referred to as single) we trained the classifiers on the union of the labeled examples from the five terrains. In the second protocol (referred to as merged) we trained multiple classifiers on each of the five terrains separately and compared the predictions of the different classifiers. For each tested candidate each of the five classifiers yields 1 (crater) or 0 (non-crater); thus each candidate can get from 0 to 5 “votes” for being a crater. For a candidate to be labeled as a crater the number of “crater” votes must exceed certain threshold. The value of the threshold is chosen such that the difference between the number of craters and non-craters is as small as possible (i.e. as close to a 50/50 split between craters and non-craters as possible). The reasoning behind this is empirical, as our observations have shown that among

the candidates generated by Cratermatic for the Moon, roughly 50 percent are craters. From Table 1 it is clear that the C4.5 algorithm and the merged protocol yield the best results.

**Future work:** The next step is to perform a similar comparison of different machine-learning methods for the two remaining categories of craters. Once we are confident in our classifiers, they will be applied to all the tiles and the results will be combined into a global catalog. The catalog will be reviewed manually and some large and/or degraded craters will be added to it. This is because the algorithm can perform poorly when detecting craters that are substantially degraded or very large.

**Conclusions:** We have established that the methodology of automatically identifying craters from Martian DEM [2] can be applied to the lunar DEM with minimum modifications to the depression-finding algorithm parameters and the classification technique. We expect that the LOLA team will release a 128 pixels/degree DEM and possibly a higher resolution DEM in the future. Our method is ready to be applied to those higher resolution DEMs and will find smaller craters efficiently and in the global scale. Finally, using our new catalog we will produce global depth/diameter maps for the Moon.

#### References:

- [1] Andersson L. B. and Whitaker B. A. (1982) *NASA Reference Publication 1097*.
- [2] <http://imbrium.mit.edu/>
- [3] Stepinski T. F. et al. (2009) *Icarus*, 203(1), 77-87.
- [4] Mendenhall M. P. (2006) <http://cratermatic.sourceforge.net>.
- [5] Quinlan R. (1993) *C4.5: Programs for Machine Learning*, Morgan Kaufmann Publishers.
- [6] Breiman L. *Machine Learning*, 45(1), 5-32.
- [7] Platt J. C. (1998) *Advances in Kernel Methods - Support Vector Learning*, MIT Press.
- [8] Hall M. et al. (2009) *SIGKDD Explorations*, 11(1)

**MINERAL CHEMISTRY AND ORIGIN OF SPINEL BEARING ROCKS IN LUNAR HIGHLAND METEORITES.** T.R. Engle<sup>1</sup>, J. Gross<sup>2</sup>, and A.H. Treiman<sup>2</sup>, <sup>1</sup>Sam Houston State University, Department of Geology Huntsville, TX 77340 (tre003@shsu.edu), <sup>2</sup>Lunar and Planetary Science 3600 Bay Area Boulevard Houston TX 77058.

### Introduction:

Spinel rich rocks are rare in returned lunar samples as well as in lunar meteorites. However, rocks with abundant spinel,  $(Mg,Fe)Al_2O_4$ , have been reported recently on the lunar farside [1]. Gross and Treiman [2] also report a 'new' spinel-rich rock fragment in lunar meteorite ALHA81005 (containing 30vol% spinel) that could be part of the rock type reported by [1]. Spinel rich rocks are important because they may have formed deep in the lunar crust. However, their origins are basically unknown.

The mechanism(s) of forming spinel-rich rocks are not clear. A very aluminum rich source is needed to produce spinel rich rocks. On the Earth they can be formed by metamorphic processes that include clay-rich (and therefore aluminous rich) lithologies. These processes are unlikely to have happened on the Moon since the volatile abundance is too low and chemical weathering could not take place to form clay rich rocks, which are needed in the first place.

However, they could form by igneous processes. Spinel-rich compositions are unlikely to be primary liquids generated in the lunar basaltic system, as basaltic and corundum-normative (including spinel-rich) melts are separated by a thermal divide (e.g., [3]). However, spinel rich rocks might form by accumulation of spinel [4-5] from olivine-plagioclase melts, as might be produced by impact melting [5-7]. On the other hand, spinel-rich rocks could be restites, residual after a basaltic melt was removed from a partially melted rock rich in olivine and plagioclase ([8]; see [5]).

To test these hypotheses we investigated the origin of the spinel rich clasts through detailed petrography, mineral-chemical analyses, thermochemical calculations, and laboratory experiments. The experiments focused on the spinel+melt field near the join olivine-plagioclase, as model for formation of spinel-rich rocks from crustal melts, igneous and impact. Mineral thermobarometry will constrain the P and T of equilibration, and thus the clasts' depths and settings in the Moon. From our experimental and thermochemical results on lunar spinel rich clasts we will place constraints on the origin and formation mechanisms/conditions of spinel rich rock lithologies in lunar highlands.

### Sample and Methods:

ALHA 81005, found in 1982, is a polymict, anorthositic regolith breccia from the lunar highlands, pos-

sibly from the farside [9-10]. The clasts in this meteorite include anorthosites, granulites, mineral grains, breccias, impact melts, impact glasses, and mare basalts, set in a glassy agglutinitic matrix [2]. In this study we analyzed 2 spinel-rich clasts [2] (e.g. Fig. 1)

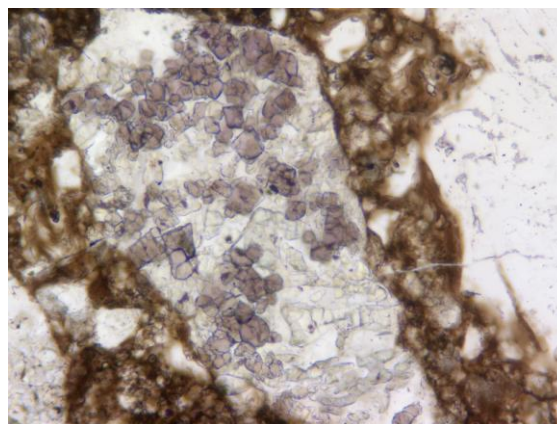


**Fig. 1:** Plane polarized image of clast 2, 0.5 cm across (c/o K. Rahilly). Note the purple spinel grains.

from the polished thin section ALHA81005,9.

### Chemical Analyses and Imaging:

Backscattered electron (BSE) images, quantitative analyses of mineral composition and element maps were obtained with the Cameca SX100 electron microprobe (EMP) at NASA Johnson Space Center (JSC). Quantitative analyses were obtained by wavelength dispersive spectrometry. Operating conditions were: 15-20kV accelerating voltage, 15-20nA beam current, focused electron beam (1 $\mu$ m in size) and peak and background counting times of 20-40s per element. Data quality was ensured by analyzing the standard materials as unknowns.

BSE images and element maps were used to determine the textural characteristics and the modal mineral abundance of the clasts using the multispectral image processing code MultiSpec (see [11]). Counts at characteristic  $K\alpha$  energies for Mg, Ca, Fe, and Al were collected in wavelength-dispersive mode (WDS) at a 15 kV accelerating potential and 40 nA beam current. At each point, X-ray counts were acquired for 60 milliseconds, and the grids of data rendered as images.

### Experiments:

Experiments were done on a composition on the forsterite-anorthite join in the system CaO-MgO- $Al_2O_3$ - $SiO_2$  (CMAS), see Table 1. The starting material was made from a homogenized mixture of element oxides and  $CaCO_3$ . It was subsequently fired at 1580 $^{\circ}$ C at 1 atm to produce a homogeneous anhydrous glass.

The glass was ground to powder, remixed to ensure homogeneity and stored in a desiccator. One bar experiments were conducted in a Lindberg Box Furnace in the laboratories of the NASA ARES division, JSC. About 125 mg of the powder was loaded into five 4cm long Pt-Au capsules (diameter ~0.5cm) and melted at 1520°C for 24 hours to ensure homogeneity and equilibrium. The samples were then cooled to the run temperature and allowed to equilibrate for 18-24 hours before quenching in air or water.

**Table 1:** Starting composition for experiments.

	Starting Composition (%)
SiO <sub>2</sub>	43.06
Al <sub>2</sub> O <sub>3</sub>	24.13
MgO	19.5
CaO	13.31

#### Mineral Equilibria Calculations:

Pressures and temperatures of equilibration for mineral assemblages in spinel-bearing lunar materials were calculated using empirical relations from the literature, and the computer code THERMOCALC [12], following [13]. THERMOCALC uses the self-consistent thermochemical database of [14] as updated and with a self-consistent set of activity-composition relationships (a-X) for minerals [14, 15].

#### Results:

##### Analytical:

We analyzed two spinel-bearing clasts; clast 2 is a spinel-rich troctolite, Fig.1 [2] and clast 19 is a spinel bearing granulite. All mineral phases are homogeneous; Table 2 shows representative mineral compositions. Using an X-ray mapping method [11], we determined modal mineral abundances (volume) in clast 2 as 29% spinel, 47% plagioclase, 16% olivine, and 7% pyroxene (Fig. 2). For clast 19, we did not obtain mineral abundances but estimate that it contains less than 2 % volume of spinel.

**Olivine** grains in both clasts are equigranular, and range in size from 10 to 50µm. Compositionally, olivine in clast 2 ranges from Fo74 to Fo76 and from Fo78 to Fo80 in clast19.

**Pyroxenes** are present in both clasts. Clast 2 contains two pyroxene grains, 40 - 90µm across. Their compositions are somewhat variable, Wo4-12En70-76Fs18-22. Scattered high-Ca spots in those pyroxenes (Fig. 2) are probably exsolved augite, but have not been analyzed. In clast 19, pyroxene occurs in grain sizes and proportions, as does olivine, with compositions from Wo4-8En71-80Fs16-19.

**Plagioclase** occurs as interstitial phase and is heavily cracked. The composition of the plagioclase is relative

constant in both clasts, ranging from An95-97 in clast 2 and from An94-98 in clast 19.

**Spinel** occurs as subhedral to granular mineral grains ranging from 10-60µm in size in both clasts and is an Mg-Al spinel with less than 13wt% of Cr<sub>2</sub>O<sub>3</sub> and about 0.5 wt% TiO<sub>2</sub>.

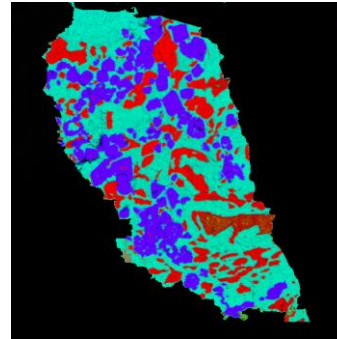
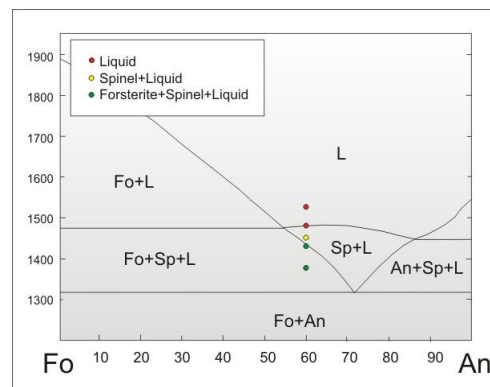


Figure 2: Color-coded element map of Clast 2 (see Fig. 1), created with MultSpec®. Element colors are Al-blue, Mg=red, Ca=green. Minerals appear as: spinel = purple; plagioclase = bluish green; olivine = bright red; pyroxenes = dark red

Experimental:

The 1 bar experiments were quenched at 1530°C, 1481°C, 1450°C, 1430°C and 1380°C. Figure 3 shows the starting composition on the Fo-An phase diagram (reference), and we confirm those results – spinel crystallizes first between 1481 and 1450 °C, and olivine begins to crystallize near 1430 °C. Mineral abundances were calculated based on mass balance calculations from the melt (Fig. 4). Spinel was observed in the 1450 °C charge at an abundance of < 1% (from mass balance); the lowest temperature run, at 1380 °C, contained only ~ 7 mass% spinel.



**Figure 3:** Phase relations in forsterite-anorthite (Fo-An) in CMAS, phase boundaries from [20]. Composition, temperatures, and results of our experiments as colored circles.

##### Phase Equilibria:

The mineral assemblages of the clasts constrain the temperatures and pressures of their solid-state (metamorphic) equilibration. For clast 2, spinel-orthopyroxene equilibria suggest an equilibration temperature near 500°C [16], although the calibration of [17] yields temperatures near 1000°C. The Al content of orthopyroxene in a spinel-bearing peridotite is a robust thermometer, as it is nearly independent of P and of Fe/Mg [18,19], see Figure 5. The orthopyrox-

enes in clasts 2 and 19 average  $\sim 0.067$  and  $\sim 0.048$  Al per formula unit respectively, and so imply equilibration at temperatures near  $600^\circ\text{C}$  and  $525^\circ\text{C}$ , Figure 5.

The pressures of equilibration are constrained by chemical reaction of plagioclase-peridotite to spinel-peridotite, with spinel at higher pressure. The clasts contain all relevant minerals (ol, opx, cpx, pl, sp), and we have calculated the location of that equilibrium for the Mg# of clasts 2 and 19. Temperatures from Al-in-opx and these equilibria constrain both clasts to have equilibrated near zero pressure (Fig. 5).

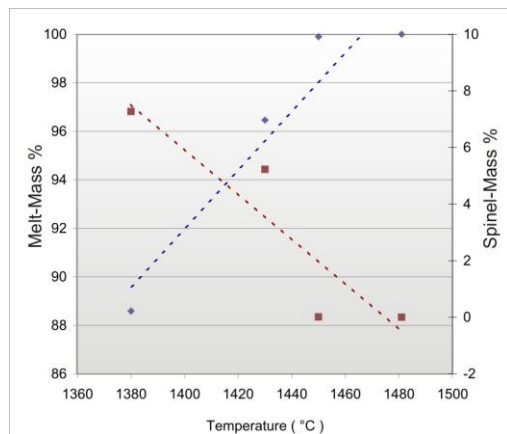


Fig. 4: Spinel (red dots and line) and melt (blue dots and line) abundance plotted vs. temperature calculated based on mass balance.

### Conclusions:

Our experiments on melting and crystallization confirm the results of earlier work [3,20] on phase equilibria on the forsterite-anorthite join, and confirm the inferences of [4,5] that lunar rocks rich did not form directly as igneous or impact melts, but must represent accumulations of spinel. Our results on the metamorphic (post-igenous) equilibration of two spinel-bearing clasts in lunar meteorite ALHA81005 give relatively low temperatures ( $\sim 600^\circ\text{C}$ ) and pressures near zero, i.e. near the lunar surface. Together these results a possible formation scenario for these spinel-rich lunar rocklets. A large meteoroid impact into a lunar site rich in olivine and anorthite produced a large pool of impact melt, probably in its impact crater (i.e. at low pressure). As that melt cooled, spinel crystallized first, and sank to produce cumulates rich in spinel. These cumulates crystallized fully, and cooled slowly to give blocking temperatures near  $600^\circ\text{C}$ . Later impact events liberated fragments of this rock and deposited them on the Moon's surface.

### Acknowledgments:

We are grateful to A. Peslier and L. Le for assistance with the EMP analyses and especially to L. Lee for her patience and assistance with the experiments.

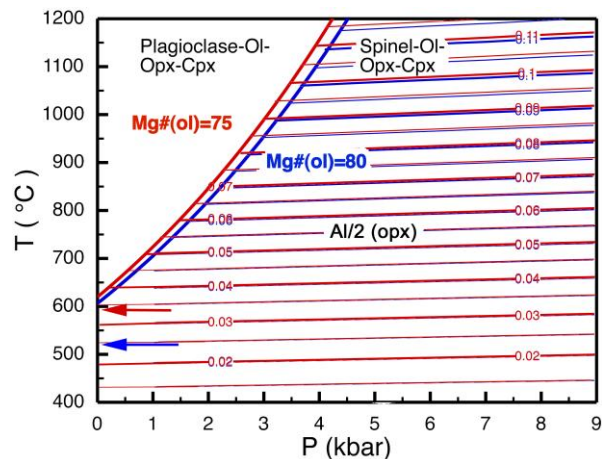


Fig. 5: Al content of orthopyroxene (thin lines) and equilibrium locations for plagioclase-spinel peridotite, for An95 plagioclase, calculated via THERMOCALC. Red: Mg#(Ol)=75 (clast 2); blue: Mg#(Ol)=80 (clast 19). Arrows indicate temperature inferred from the average composition and the Al-in-orthopyroxene isopleths for clast 2 (red) and clast 19 (blue).

Table 2: Representative mineral analyses, clasts 2 and 19.

	Clast2		Clast19	
	spinel	pyroxene	spinel	pyroxene
Na <sub>2</sub> O	0.04	0.00	0.01	0.02
MgO	16.74	26.38	15.54	28.76
Al <sub>2</sub> O <sub>3</sub>	63.57	1.16	52.85	1.18
SiO <sub>2</sub>	0.07	54.57	0.03	54.49
K <sub>2</sub> O	0.00	0.00	0.01	0.00
CaO	0.10	4.04	0.04	2.03
TiO <sub>2</sub>	0.45	0.42	0.55	0.55
Cr <sub>2</sub> O <sub>3</sub>	3.52	0.23	12.67	0.53
MnO	0.08	0.21	0.18	0.29
FeO	15.45	12.72	17.14	12.18
NiO	-	-	0	0.02
Total	100.03	99.76	99.02	100.04

### References:

- [1] Pieters C et al., (2010) *41<sup>st</sup> LPSC*, Abstr. 1854. [2] Gross J and Treiman AH (2010) *41<sup>st</sup> LPSC*, Abstr. 2180. [3] Presnall DC et al. (1978) *Contrib. Mineral. Petrol.* 66, 203 [4] Prinz M et al. (1973) *Science* 179, 74 [5] Marvin U et al. (1989) *Science* 243, 925. [6] Walker et al. (1973); [7] Treiman A.H. et al. (2010) *MaPS* 45, 163. [8] Taylor LA & Bence AE (1975) *Proc. Lunar Sci. Conf. 6th*, 1121 [9] Goodrich C et al., (1984) *Proc. LPSC 15th*, C87. [10] Korotev R (2005) *Chemie Erde* 65, 297. [11] Maloy A & Treiman AH (2007); [12] Powell R et al. (1998) *J. Metam. Geol.* 16, 577. [13] Schmädicke E. (2000) *J. Petrol* 41, 69. [14] Holland TJB & Powell R (1990) *J. Metam. Geol.* 8, 89 [15] Holland TJB & Powell R (2003) *Contrib. Mineral. Petrol.* 145, 492. [16] Ballhaus C et al. (1991) *Contrib. Mineral. Petrol.* 107, 27. [17] Liermann HP & Ganguly J (2007) *Contrib. Mineral. Petrol.* 154, 491. [18] Gasparik T (1987) *Contrib. Mineral. Petrol.* 96, 357. [19] Gasparik T. (2000) *J. Geol.* 108, 103. [20] Osborne EF & Tait DB (1952) *Am. Jour. Sci., Bowen Special*, 413.

**PROPERTIES OF LUNAR POLAR DEPOSITS REVEALED BY THE MINI-RF IMAGING RADAR ON THE CHANDRAYAAN-1 AND LUNAR RECONNAISSANCE ORBITER MISSIONS.** Joel W. Hecker<sup>1</sup> and Paul D. Spudis<sup>2</sup>, <sup>1</sup>University of Cincinnati Department of Geology, 2600 Clifton Ave., Cincinnati, OH 45221 (joelwhecker@gmail.com), <sup>2</sup>Lunar and Planetary Institute, 3600 Bay Area Blvd., Houston, TX 77058.

**Introduction:** Two lunar orbiting satellites, the Indian Chandrayaan-1 and the Lunar Reconnaissance Orbiter (LRO), have been mapping the polar and equatorial regions of the Moon using imaging radar. The goals of this experiment are to map and characterize the backscattering properties of polar deposits, with the aim of identifying deposits of water ice, if present [1]. The Chandrayaan-1 Mission mapped the Moon from November 2008 until August 2009, while the LRO Mission has been mapping the Moon continuously since June 2009. The Chandrayaan-1 spacecraft contained the Miniature Synthetic Aperture Radar (Mini-SAR) to collect S-band (12.6 cm wavelength) SAR images of the poles, along with some selected non-polar regions for calibration purposes, both at 150 m resolution [2]. The LRO is using the Mini-RF instrument to map the poles and other select regions of the lunar surface at two resolutions (150 m and 30 m) and two frequencies (12.6 cm and 4.5 cm wavelengths) [3]. With both data sets, the diffuse radar backscatter properties of the surface are measured and characterized by the circular polarization ratio (CPR), which is the ratio of the power of the received signal of the same sense transmitted over the opposite sense. Normal lunar surface has low CPR (on the order of 0.3-0.4), but CPR values are higher for coarse, blocky materials, as the radar signal may bounce multiple times, returning in both same and different senses than were transmitted [1].

The polar regions of the lunar surface have significant exploration potential, but until recently, have remained largely unstudied. Using this new radar data in conjunction with the previously studied non-polar regions, it will be possible to characterize the reflection properties of different types of terrain and surface deposits. This in turn, will help with understanding their likely physical make up and composition. Numerous studies have indicated the possible presence of water ice in permanently dark areas near the poles [e.g., 1, 4, 5]. Although some data indicates such ice is present [e.g., 6], other data sets are inconclusive [e.g., 7]. This work is designed to fully characterize and categorize the polar deposits, in order to decipher some of the mysteries of the polar deposits, including the possibility of large amounts of water ice.

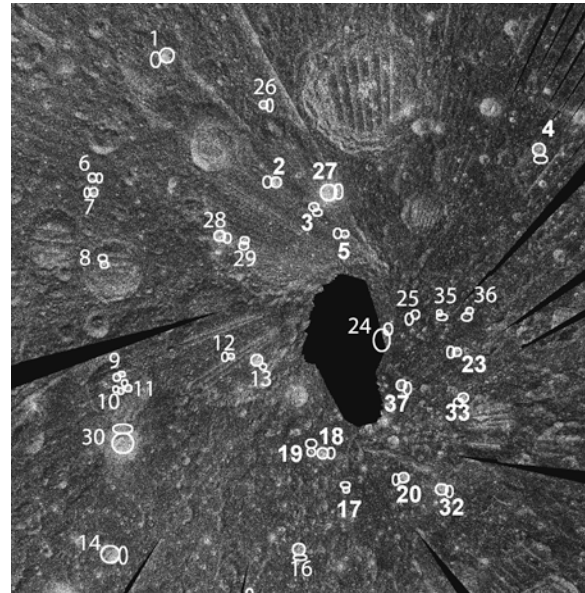


**Fig. 1.** Mini-RF mosaic of the North Pole of the Moon showing craters of interest (image covers  $\sim 78^\circ\text{N}$  to pole).

**Method:** MRF image data was processed by the MRF SAR processor at APL. This data was used to make maps of CPR. Specific, individual craters having high CPR were identified on polar mosaics and analyzed using the Adobe Photoshop and Image J image processing programs. Our aim was to thoroughly characterize and collect complete representative data for both the “normal” fresh craters (i.e., those having high CPR values both inside and outside their rims; see [4]) and the “anomalous” craters (i.e., those having high CPR only inside their rims). The CPR value of the crater interior was measured and data compiled for all pixels both within the crater rim and for representative deposits exterior to it. A histogram of CPR values was produced, showing the frequency of each CPR value within the specified crater. The same procedure was used for an area directly outside the crater, in order to show the differences in CPR of the interior and exterior of craters, for both fresh and anomalous craters [4].

The CPR data was collected for a representative set of craters near polar regions and some selected non-polar regions for direct comparison, in both the Chandrayaan-1 and LRO data. From the sum of the individual CPR values for each crater, the mean CPR value and standard deviations were calculated, for the interiors and exteriors separately. In addition, vari-

ous statistical properties were computed, including geometric means, standard skewness and standard kurtosis. These parameters were compared between and among groups to determine clustering or distinctive tendencies, which might indicate the possible origin of the surface deposits.

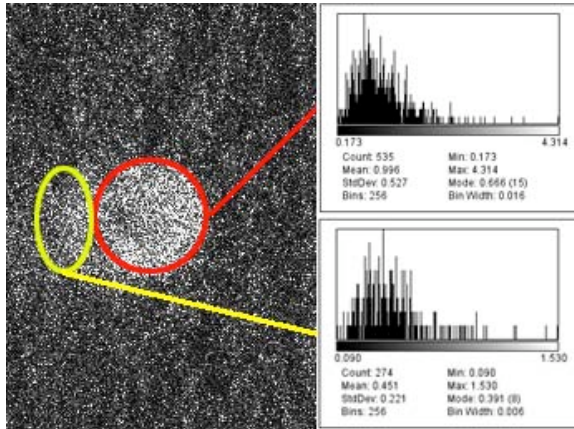


**Fig. 2.** North Polar anomalous crater (2) from Mini-RF data, showing widely differing mean CPR values and offset histograms for interior and exterior of the crater rim crest.

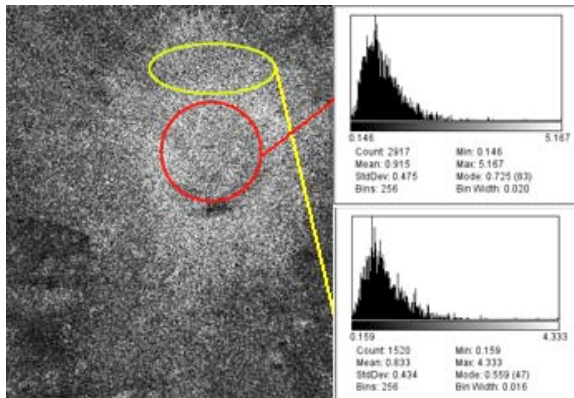


**Fig. 3.** North Polar fresh crater (30) from Mini-RF data, showing similar mean CPR values and data distributions for interior and exterior of the crater rim crest.

**Results:** The highest CPR values occur, on average, in the interiors of fresh craters, followed closely by the interiors of anomalous craters. The high CPR value in the fresh craters is probably a result of rough and blocky terrain characterized by fresh ejecta from crater impacts [4, 8]. The interiors of anomalous craters have a mean CPR value approximately two times (1.89) the value of the exterior, whereas the mean CPR values for the interiors of fresh craters are only slightly greater (1.16) than the exteriors. Other craters have an intermediate ratio between interior and exterior CPR (1.5), which falls into a gray area

between the classification of anomalous and fresh craters.

Our analysis of other statistical parameters likewise shows separation of the two classes. For example, plots of Skewness v. kurtosis (Fig. 4) show that the interiors of the two classes form two sub-parallel offset trends, suggesting that the two classes have different data properties and possibly, different origins.

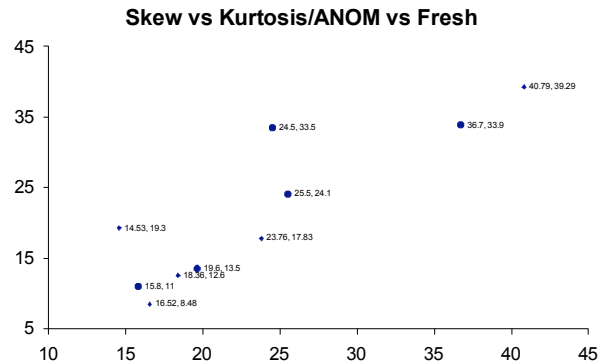


**Fig. 4.** Skewness (horizontal axis) and kurtosis (vertical axis) of the interiors (only) of the two groups (large dots: anomalous; small dots: fresh) of high CPR craters. Slight offset in data trends suggest that the two groups form distinct populations.

**Discussion:** As a crater erodes and degrades with age, the interior and exterior deposits should become more subdued at a similar rate, which would lead to comparable CPR values of both the interior and exterior deposits of the crater. This relation is actually seen for most lunar craters, with fresh craters being one end member, in which high CPR is found inside and outside the rim. However, the anomalous craters show continued high CPR inside, but not outside their rims. In addition, maps of solar illumination data [9, 10] and temperature measurements from the LRO DIVINER instrument [11] indicate that these anomalous craters all have interiors in sun shadow and very low surface temperatures (less than 100 K). Our results suggest that these anomalous craters do indeed have deposits that differ from those of fresh craters. In conjunction with other information, such as the coincidence of these anomalous craters with modeled locations of ice based on Lunar Prospector neutron spectrometer data [4], our results support the idea that these deposits are composed of water ice. Misclassification of craters is possible due to human error, or the Moon could be more complicated than the model indicates. For example, a fresh polar crater with ice would not fit within our classification set.

An elevated CPR might be caused by both surface roughness and/or ice; this classification system can not determine from which. High CPR is a necessary, but insufficient conditional indicator for the presence of nearly pure water ice.

**Conclusions:** The average temperature at the polar regions is approximately 30 K [11], the bottom of the craters are in permanent darkness [8, 9], and there are decent amounts of mobile water in the higher latitudes of the moon [12, 13]. Based on this, we have concluded that ice is causing the CPR differences. In order to have this volume scattering CPR enhancement, the ice must be tens of wavelengths (~2-3 m) thick [1, 4, 13]. It is likely, but not certain, that ice is causing this CPR enhancement. At this point, it is only known that there are definite differences between the polar anomalous craters, and the fresh impact craters on the lunar surface. Continued study of

these features will yield additional constraints on their origins and formational mechanisms.

**References:** [1] Spudis P.D. (2006) *The Space Review* <http://www.thespacereview.com/article/740/1> [2] Spudis P.D. et al. (2009) *Current Science* **96**, no. 4, 25 Feb. 2009. [3] Nozette S. et al. (2010) *Space Sci. Reviews* **150**, 285-302 [4] Spudis, P.D., et al. (2010) *Geophys. Res. Letters* **37**, L06204, doi:10.0129/2009GL042259 [5] Hagfors T. and J.V. Evans, *Radar Astronomy* 219-271, McGraw-Hill, New York, 1968. [6] Colaprete T. et al. (2010) LCROSS results, *LPSC 41*, 2335 [7] Mitranov I. et al. (2010) LEND results, *LPSC 41*, 2250. [8] Horz F. et al. (1991) *Lunar Sourcebook*, Chap. 4, 61-120. [9] Bussey B. et al. (2005) *Nature* **434**, 842. [10] Bussey B. et al. (2010) *Icarus* **208**, 558-564. [11] Paige D. et al. (2010) DIVINER, *LPSC 41*, 2267 [12] Pieters C., et al. (2009) *Science* **326**, 568-572 [13] Thompson T.W. et al. (2008) *Lunar Planet. Sci.* **XXXIX**, 1023

**Table 1.** Selected Properties of Some Polar Craters

Crater Number	F/A	Ext. Mean CPR	Int. Mean CPR	INT-EXT	INT/EXT
2NL	A	0.451	0.996	0.55	2.21
14NL	A	0.457	0.842	0.39	1.84
15NL	A	0.545	1.073	0.53	1.97
16NL	A	0.435	0.875	0.44	2.01
17NL	A	0.422	0.762	0.34	1.81
18NL	A	0.519	0.971	0.45	1.87
19NL	A	0.419	0.843	0.42	2.01
20NL	A	0.389	0.872	0.48	2.24
<b>Anomalous AVG</b>	A	<b>0.462</b>	<b>0.891</b>	<b>0.44</b>	<b>1.89</b>
28NL	F	0.766	0.928	0.16	1.21
29NL	F	0.652	0.931	0.28	1.43
30NL	F	0.833	0.915	0.08	1.10
31NL	F	0.846	0.92	0.07	1.09
32NL	F	0.737	0.881	0.14	1.20
33NL	F	0.825	1.011	0.19	1.23
34NL	F	0.708	0.814	0.11	1.15
<b>Fresh AVG</b>	F	<b>0.794</b>	<b>0.926</b>	<b>0.12</b>	<b>1.16</b>

## INVESTIGATION OF ORTHOPYROXENE DIVERSITY IN HOWARDITE METEORITES.

K. N. Johnson<sup>1</sup>, D. W. Mittlefehldt<sup>2</sup>, and J. S. Herrin<sup>2</sup>, <sup>1</sup>Youngstown State University Department of Chemistry, Youngstown, OH 44555-3663, (knjohnson01@student.yzu.edu), <sup>2</sup>NASA–Johnson Space Center, Houston, TX 77058 (david.w.mittlefehldt@nasa.gov, jason.s.herrin@nasa.gov)

**Introduction:** The howardite, eucrite and diogenite (HED) family of meteorites is considered to originate from a single parent asteroid, 4-Vesta [1]. Eucrites are meteorites thought to represent the basaltic layer of the asteroid while diogenites represent the inner magma plutons. These meteorite groups differ mineralogically, eucrites being comprised mostly of pigeonite and plagioclase while diogenites are dominated by orthopyroxene with minimal quantities of olivine and chromite [2]. These two meteorite groups are related through howardites, defined as a polymict breccia of eucritic and diogenitic fragments mixed on the surface of the parent asteroid. Warren et al. [3] suggest that the howardite group should be further divided into two types: regolithic and fragmental. Regolithic howardites have higher noble gas content that correlate with solar wind exposure, contain a mixing ratio of eucrite and diogenite of ~ 2:1 and are richer in siderophile elements, such as Ni. These characteristics are a result of originating from ancient, well-mixed regolith. Fragmental howardites show minimal evidence of regolithic processing and are suggested to have originated as more recently formed polymict breccias [3].

Our work tests Warren's hypothesis by examining the chemical differences of orthopyroxene (diogenite) grains within 8 different howardite samples. We posited that regolithic howardites would contain orthopyroxene fragments with wider ranges in minor and trace elements than would fragmental howardites formed by mixing of more limited source rocks.

As hypothesized by Warren et al. [3], some howardites are regolithic in origin while others are not. Simply because the meteorite is a mixed breccia does not mean that it originated as part of the active regolith at the surface of the parent asteroid. The purpose of developing a method to differentiate regolithic and fragmental howardites is due to the nature of data that will be received during the Dawn mission to 4-Vesta. Data from the mission will only include analysis of the top regolith layers, making an understanding of regolithic meteorites a window into the processes of the asteroid.

**Methods:** Thick sections (150 $\mu$ m) were acquired from the US Antarctic meteorite collection for 8 howardite samples (CRE 01400, PCA 02066, EET 87513, EET 99408, PRA 04401, QUE 97001, LAP 04838, SAN 03472).

Companion thin sections of the listed meteorites were examined using optical methods. Petrographic descriptions were recorded and compared with XRF bulk analysis data [4].

Images of the thick sections (for example, Figs. 1 and 2) were taken using the JSC 5910LV scanning electron microscope (SEM). Initial energy dispersive spectroscopy (EDS) data sets were used to select orthopyroxene targets for electron microprobe analysis (EMPA). EMPA data sets for each meteorite sample were taken using the JSC Cameca SX100 electron microscope. The unknown mineral samples were calibrated with JSC standard samples. Analysis was taken at an accelerating voltage = 20 kV and beam current = 40 nA. The composition of each grain was determined by averaging several EMPA data points. From those averages we will consider all grains with Wo% content of 5 mole percent or less.

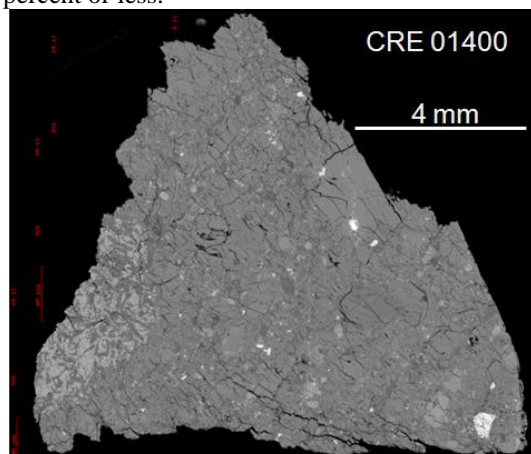


Figure 1: SEM Mosaic image of CRE 01400

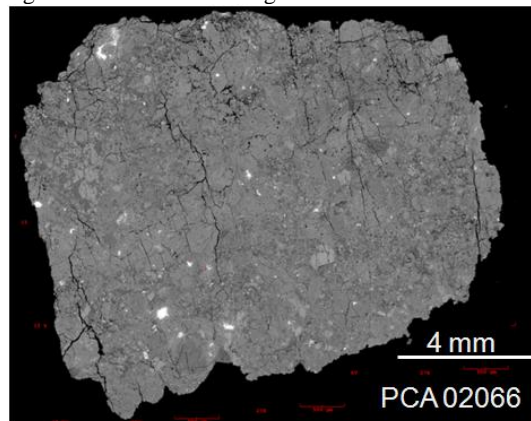


Figure 2: SEM Mosaic image of PCA 02066

**Results:**

*Petrographic Descriptions.* Observations from optical techniques were simplified and represented in Table 1 including classification under Warren's criteria for regolithic origin.

Table 1: Petrographic Regolithic Details

Sample	Fine, Medium or Coarse	Angular, subangular, rounded	Impact Melts	Chondritic Clasts	Diag. Enc	XRF Plots (NEAI)	Regolithic?	Reworked?
CRE 01400, 18	coarse	subangular	no	no	74/25	No/No	No	No
PCA 02066, 12	medium fine	angular	no	no	70/30	Yes/Yes	Yes	Yes
EET 87513, 123	medium fine	subangular	yes	no	35/65	No/Yes	Maybe	Maybe
EET 99408, 15	medium fine	rounded	yes	no	20/80	No/No	Maybe	Yes
PRA 04401, 12	coarse	angular	yes	yes	50/50	Yes/No	No	No
QUE 97001, 48	medium	subangular	yes	no	70/30	Yes/No	Maybe	No
LAP 04838, 18	medium coarse	subangular	yes	no	15/85	No/No	No	No
SAN 03472, 14	medium	subangular	yes	no	35/65	No/No	Maybe	No

*SEM and EMPA Data.* Images of orthopyroxene grains in EET 99408 and SAN 03472 (greater abundance in EET 99408) appeared zoned (Fig. 3).

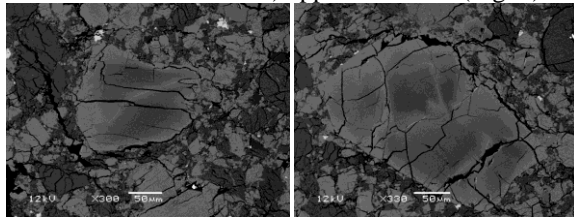


Figure 3: Examples of zoned orthopyroxene grains as observed in EET 99408.

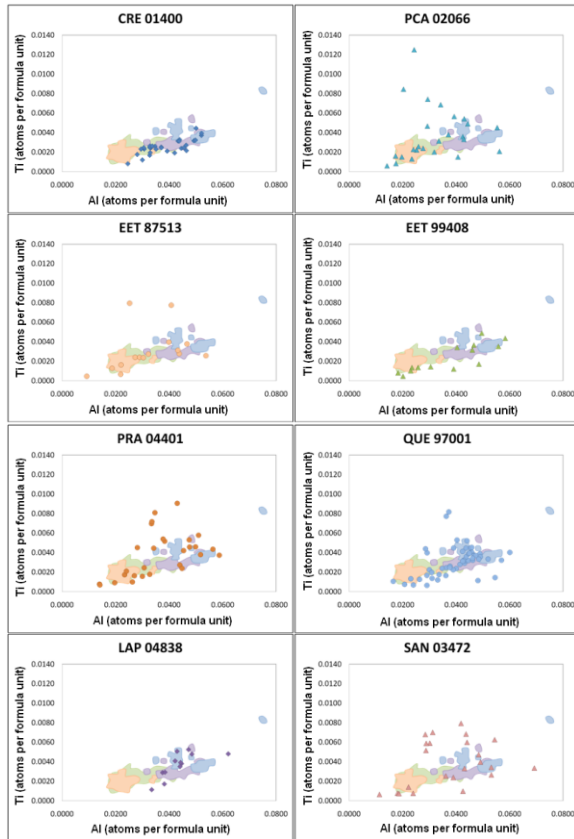


Figure 4: Plots of Ti vs. Al (in atoms per formula unit) from microprobe analysis for all 8 meteorite samples in comparison to ranges of selected diogenite meteorites:

- EETA 79002
- Roda
- Johnstown
- Yamato A

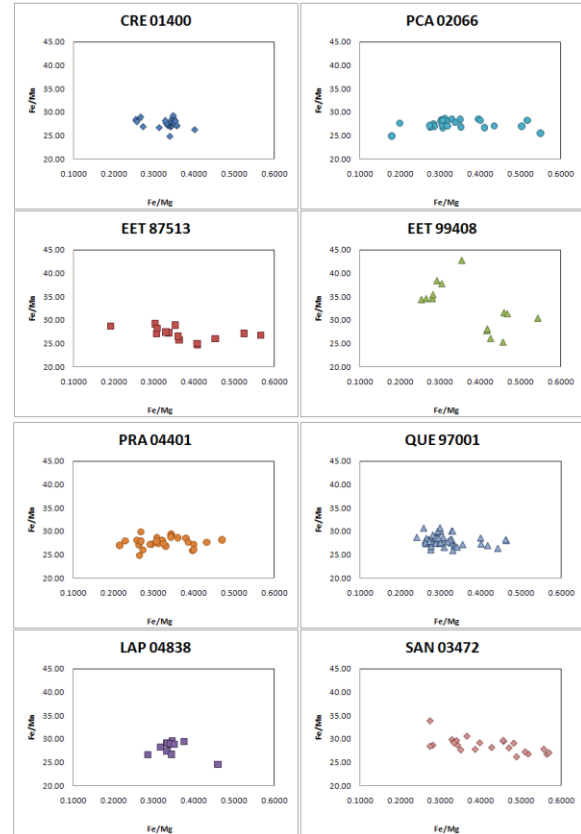


Figure 5: Plots for molar Fe/Mn vs. Fe/Mg of all 8 howardites.

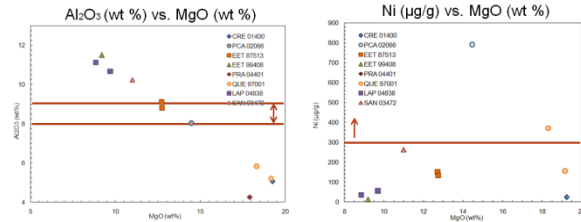


Figure 6: XRF bulk chemical analysis for studied howardites (PRA 04401 is excluded from Ni vs. Mg plot for clarity; point lies at [17.9, 4438]); ranges considered to indicate regolithic samples [3] marked in red

**Discussion:** It has been suggested that the presence of chondritic material in the form of enhanced siderophile element content could be used as an indicator of a regolithic sample [3]. However, high siderophile element contents in howardite samples alone are not conclusive evidence for regolith origin. Case in point is PRA 04401, which has a very high Ni content [4]. This meteorite contains abundant, mm-sized angular chondritic clasts. The facts that the clasts have remained angular and concentrated in one stone is an indication that the sample did not undergo extensive regolith gardening. Regolithic processes would have reduced the clast size and angularity, dispersing the chondritic material across the asteroid surface. In the case of

PRA 04401, presenting high siderophile element content as evidence of regolithic origin is incorrect. In terms of its orthopyroxene composition, PRA 04401 has significant diversity. A plot of Ti vs. Al for PRA 04401 shows a wider range in composition than typically seen in individual diogenites (Fig. 4). This suggests that it contains orthopyroxene debris from several diogenitic plutons.

For our study, the diversity of orthopyroxene grains in each meteorite sample shows some correspondence with the regolithic character of the sample from petrographic descriptions. For example, grains within CRE 01400 are very similar to one another in composition, supporting the classification of CRE 01400 as a fragmental howardite. This howardite may be the result of one large, more recent impact that was not followed by extensive mixing in the regolith of the asteroid. PCA 02066 shows a very wide diversity of orthopyroxene grains (Fig. 4), potentially caused by continued mixing of different diogenitic materials into the regolith. Coupling our pyroxene compositional data with the petrographic descriptions of each sample (Table 1), those samples that have more rounded, smaller grains correspond to regolithic environments while the samples with larger grains and less diverse chemical data did not experience as much regolithic activity.

Zoned orthopyroxene grains were observed in EET 99408 and SAN 03472 (Fig. 3). Whether or not the zoning occurred while the grains were in the matrix or before the grains joined the breccia is up to debate. Currently, it appears as though the zoning occurred before forming the breccia. By observing the smaller orthopyroxene grains in the matrix, it is observed that these grains still contain their unreacted orthopyroxene cores and have not been entirely changed. If the zoning had occurred in the matrix, based on the size of the rims on nearby larger grains, the smaller grains should have been completely converted. For SAN 03472, the chemical changes in the orthopyroxene grains would not have occurred in the current matrix. In EET 99408, zoning is observed in the interiors of some grains, and the zoned rims do not show uniform thickness around the grains, further suggesting that the zoning did not occur after incorporation with the current matrix.

Furthermore, the zoned grains in EET 99408 show anomalous compositions. They have much higher molar Fe/Mn ratios than orthopyroxene grains from other meteorite samples. This trend is correlated with their Fe/Mg ratio (Fig. 5). The compositional changes are consistent with late addition of FeO to the pyroxenes, but the process by which this was done is not clear.

**Conclusions:** Even though all howardites are polymict breccias, some appear to be regolithic while

others do not. In Figure 1 and Table 1, this point is demonstrated by CRE 01400 which, by our classification, is a fragmental howardite and exhibits few regolithic properties. The sample is comprised of subangular, large diogenitic grains which are not diverse in trace element abundance. PCA 02066 exhibits regolithic qualities with a variety of diogenite grains in a fine- to medium-grained matrix. Grains in the sample are rounded and diverse in chemical composition, impact melt clasts are common, and this meteorite has a high Ni content (Fig. 6). This meteorite exhibits evidence of “regolith gardening”.

Although we agree with Warren et al. [3] that howardites can be divided into sub-groups, to say that there exist only two such classifications is oversimplifying. Most of the howardites that we analyzed did not fall within the rigid boundaries of regolithic and fragmental howardites, but appear to be more of an intermediary stage or even a different type of regolith on the surface of 4-Vesta. At this time, we were unable to conclusively classify these howardites within the different sub-groups set forth by Warren et al. [3]. The matter of classification will need to be a process including both textural observations and chemical variation. Thus far, it appears that orthopyroxene compositions may not provide conclusive evidence regarding the regolithic character of a howardite, but they may provide important additional information that can aid in proper classification.

**References:** [1] Binzel R. P. and Xu S. (1993) *Sci.*, 260, 186-191. [2] Mittlefehldt et al. (1998) *Rev. Mineralogy*, 36, chapter 4. [3] Warren P. H. et al. (2009) *Geochim. Cosmochim. Acta*, 73, 5918-5943. [4] Mittlefehldt D. W. (2010) *LPS XLI*, 2655-2656.

**INTERACTION OF CALCITE AND SO<sub>2</sub> IN MARS PHOENIX THERMAL AND EVOLVED-GAS ANALYZER.** A. R. Koss<sup>1</sup> and B. Sutter<sup>2</sup>, <sup>1</sup>Massachusetts Institute of Technology (77 Massachusetts Avenue, Cambridge, MA 02139, arkoss@mit.edu), <sup>2</sup>Jacobs ESCG (Houston, TX 77058).

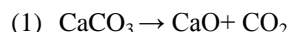
**Introduction:** The geochemical study of Mars has been guided by the search for mineral indicators of water-associated weathering. Sulfates have been a target of recent orbiter and lander investigations. Magnesium sulfate hydrates (MgSO<sub>4</sub>·nH<sub>2</sub>O) are particularly interesting for the number of naturally occurring hydration states that form only under specific chemical and thermal conditions, the characterization of which may help elucidate Mars's climatic history [1, 2]. X-ray spectroscopic analysis from the Viking [3], Pathfinder [4], and MER [5] surface missions and visible-near infrared analysis from OMEGA/Mars Express [6, 7] and CRISM/MRO [8] have suggested a global presence of magnesium sulfates on Mars (e.g. [9]).

The 2007 Phoenix Mars Lander's Wet Chemistry Laboratory (WCL) detected 1.3 (±0.5) wt.% soluble SO<sub>4</sub><sup>2-</sup> with Mg<sup>2+</sup> as the dominant counter ion [9, 10]. The suggested global presence of magnesium sulfate coupled with the WCL results indicated that the Phoenix's Thermal Evolved Gas Analyzer (TEGA) should have detected evolved SO<sub>2</sub> from MgSO<sub>4</sub> decomposition. However, TEGA detected no SO<sub>2</sub>. This suggested (counter to the WCL data) that no MgSO<sub>4</sub> species were present in Phoenix soil samples [11].

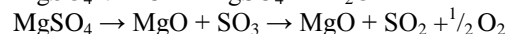
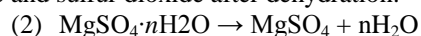
TEGA consisted of eight small calorimeter ovens coupled to a magnetic-sector mass spectrometer. Calorimetry was used to measure the temperatures and enthalpies of endothermic and exothermic phase transitions. The addition of a mass spectrometer allowed the characterization of volatiles from mineral decomposition. TEGA could reach 1000 °C, used heating rates of 5-20 °C/min, operated at 12mb pressure, and delivered evolved gases from the calorimeter to the mass spectrometer using purified N<sub>2</sub>. Samples were reheated to 1000°C one or two days after the initial analysis to determine background transitions.

TEGA results indicated reactions involving low temperature O<sub>2</sub> release, two H<sub>2</sub>O releases, and two CO<sub>2</sub> releases [12, 13]. The higher temperature (725-820°C) CO<sub>2</sub> release was interpreted as CaCO<sub>3</sub> decomposition. The soil at the landing site was estimated to contain 3-5 wt% calcite, confirmed by independent WCL measurements [13]. The presence of calcite, offers a possible explanation as to why no evolved SO<sub>2</sub> from MgSO<sub>4</sub> decomposition was detected by TEGA.

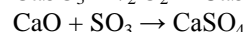
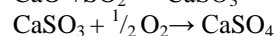
During heating, calcite decomposes to lime and carbon dioxide:



Magnesium sulfates will similarly decompose to periclase and sulfur dioxide after dehydration:



CaO generated at lower temperatures could have possibly removed the sulfur oxides generated by magnesium sulfates, forming anhydrite:



This study aimed to demonstrate that the lack of SO<sub>2</sub> in Phoenix evolved gas analysis does not necessarily constitute evidence of absence of magnesium sulfates. TEGA results could be markedly affected by reactions such as CaO scrubbing of SO<sub>2</sub>. To evaluate this possibility, we conducted thermal and XRD analyses of a range of calcite/kieserite mixtures at both ambient (1000mb) and Phoenix (12mb) operating pressures.

**Methods:** Mixtures of Iceland spar calcite (Chihuahua, Mexico) and ESTA Kieserite (Neuhof-Ellers, Germany), particle size 53-150µm, were analyzed via powder X-ray diffraction (XRD) and coupled differential scanning calorimetry/evolved gas analysis (DSC/EGA). Sample mixtures contained 0.1mmol kieserite, to which 0, 0.05, 0.1, and 0.15mmol calcite were added. An additional mixture containing 0.1mmol calcite (no kieserite present) was analyzed as a control.

DSC/EGA experiments were conducted in a setaram Ligne 96 heat flux DSC coupled to a Pfeiffer Vacuum ThermoStar GDS 301 mass spectrometer. Two pressure and carrier gas flow rate regimes were used: 1000mb with a 20scc·min<sup>-1</sup> flow rate, as a control, and 12mb with a 1scc·min<sup>-1</sup> flow rate, to emulate Phoenix TEGA operating conditions. Each sample mixture was heated from 30 to 1100°C at 20°C·min<sup>-1</sup>, cooled to 30°C and allowed to equilibrate, and reheated to 1100°C. Evolved gases were carried in N<sub>2</sub> to the mass spectrometer. Analyses were replicated, and the average DSC heat flow and mass spectrometer ion currents for fragments m/z 18 (H<sub>2</sub>O), 44 (CO<sub>2</sub>), and 64 (SO<sub>2</sub>) were calculated. The DSC heat flow curve during the sample reheat was taken as the baseline and subtracted from the initial heating curve. SO<sub>2</sub> ion current minus the background was integrated to give total counts

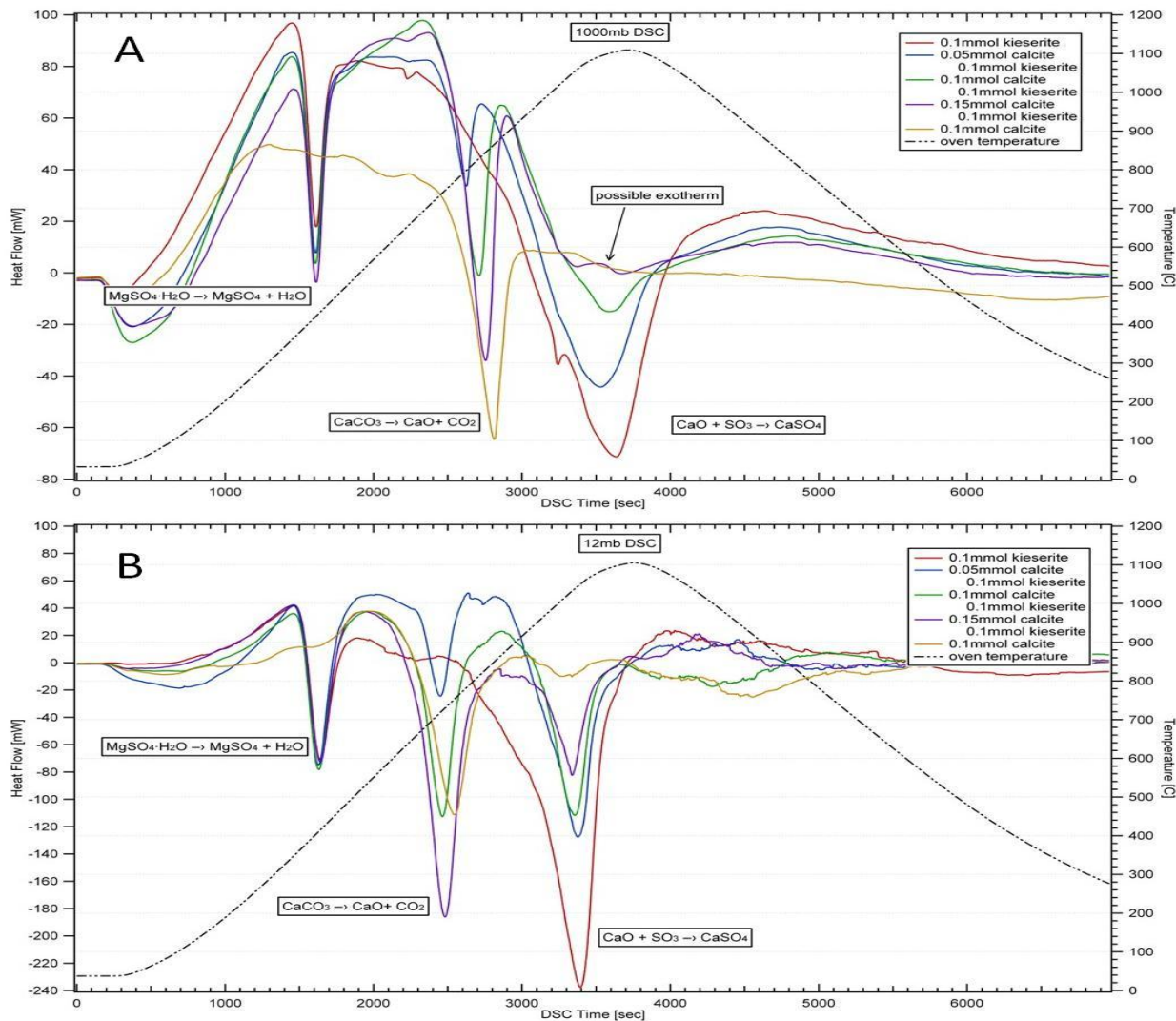


Fig. 1 (above). DSC heating curves for calcite/kieserite mixtures. A. 1000mb experiments. B. 12mb experiments.

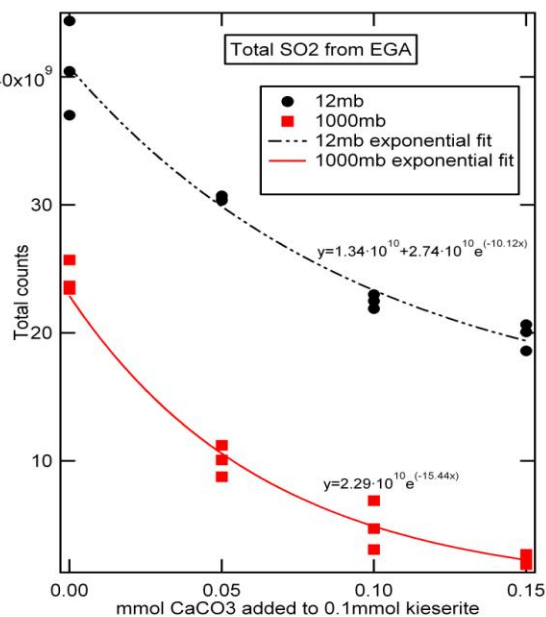


Fig. 2 (left). Dependence of total SO<sub>2</sub> evolved on mols calcite in sample mixture.

during each experiment, a proxy for total mols SO<sub>2</sub> released.

Phase changes during heating and reaction products were characterized in an AntonXRK 900 non-ambient cell using a PANalytical X'Pert Pro powder X-ray diffraction (XRD) unit. To ensure MgSO<sub>4</sub> decomposition occurred within the operating range of the instrument (<900°C), XRD experiments were conducted under low pressure conditions (10<sup>-2</sup>mb). Sample mixtures of grain size 53-150µm containing 100% kieserite, 100% calcite, and a 1:1 molar ratio of calcite and kieserite were heated at 20°C/min from 25 to 900°C, with measurements taken every 10°C in the MgSO<sub>4</sub> decomposition range (750-900°C) and every

25°C elsewhere. These analyses were replicated using <53µm grain size to provide better resolved peaks.

**Results and Discussion:** 1000mb DSC experiments showed clear endothermic peaks with onsets between 385°C, 740-790°C, and 1000-1070°C (Fig. 1a). Associated EGA showed H<sub>2</sub>O, CO<sub>2</sub>, and SO<sub>2</sub> release accompanying the peaks; these transitions were identified as kieserite dehydration, calcite decomposition, and MgSO<sub>4</sub> decomposition, respectively. The apparent enthalpy of the MgSO<sub>4</sub> decomposition peak decreased with increasing mols of calcite. This is consistent with the hypothesis that the exothermic reaction  $\text{CaO} + \text{SO}_3 \rightarrow \text{CaSO}_4$  ( $\Delta H^\circ = -403.75 \text{kJ}\cdot\text{mol}^{-1}$ ) occurs in conjunction with the endothermic decomposition  $\text{MgSO}_4 \rightarrow \text{MgO} + \text{SO}_3$  ( $\Delta H^\circ = 264.52 \text{kJ}\cdot\text{mol}^{-1}$ ). For 100% yield of 1:1 molar mixture, the expected peak is exothermic; our system began to show a possible exothermic transition occurring in the 0.15mmol calcite, 0.1mmol kieserite mixture at 1000mb.

Levels of detectable SO<sub>2</sub> decreased exponentially with increasing mmols CaCO<sub>3</sub> added to 0.1mmol kieserite (Fig. 2).

Corresponding 12mb DSC results were similar, showing clear peaks produced by kieserite, calcite, and magnesium sulfate decomposition (Fig. 1b). Decomposition onset temperatures were shifted lower relative to 1000mb trials, occurring between 360-370°C, 650-660°C, and 920-960°C, respectively. Reduced decomposition temperatures and increased enthalpies were expected from previous TEGA calibration studies [14].

Relative to 1000mb regime experiments, total levels of detected SO<sub>2</sub> at 12mb were higher, and the decrease per increment CaCO<sub>3</sub> added was less (exponential constant of -15.44 at 1000mb versus -10.12 at 12mb). The low instrument operating pressure (causing gas evolution to be more entropically favorable) may be conducive to SO<sub>2</sub> escape from the sample, despite the lower carrier gas flow rate used at 12mb.

XRD analysis confirmed the low temperature conversion of kieserite to MgSO<sub>4</sub>, intermediate temperature calcite decomposition to CaO, and high temperature formation of MgO from MgSO<sub>4</sub>. Anhydrite formation was seen at high temperature in the 1:1 molar mixture of calcite and kieserite. XRD detection of anhydrite as a major product of thermal analysis of calcite-kieserite mixtures established the occurrence of the reaction  $\text{CaO} + \text{SO}_3 \rightarrow \text{CaSO}_4$ .

**Summary and Conclusions:** Combined results from thermal and x-ray analysis demonstrate that CaO produced by calcite decomposition in Phoenix soil samples can conceal thermal and EGA signatures of magnesium sulfates under Phoenix TEGA operating conditions. Our data suggest that if both calcite and

kieserite were present in Phoenix soil samples, kieserite would not have been detected.

The results of this study highlight the need for a more comprehensive thermal database of possible soil components and their behavior in spacecraft instrumentation. Mineral interactions during thermal analysis should be important considerations for interpretation of both data from Phoenix TEGA and data to be collected from the Mars Science Laboratory Sample Analysis instrument suite, scheduled to launch in 2011.

**References:** [1] Vaniman D. T. et al. (2004) *Nature*, 431, 663–665. [2] Roach L. H. et al. (2009) *JGR*, 114, E00D02. [3] Clark B. C. (1982) *JGR*, 87, 10059-10067. [4] Wänke H. et al. (2001) *Space Sci. Rev.*, 96, 317-330. [5] Clark B. C. (2005) *Earth Planet. Sci. Lett.*, 240, 73-94. [6] Gendrin A. et al. (2005) *Science*, 307, 1587-1590. [7] Langevin Y. et al. (2005) *Science*, 307, 158401586. [8] Roach et al. (2007) *LPS XXXVIII*, Abstract #1970. [9] Kounaves S. P. et al. (2010) *Geophys. Res. Lett.*, 37, L09201. [10] Kounaves S. P. et al. (2010) *JGR*, 115, E00E10. [11] Golden D. C. et al. (2009) *LPS XXXX*, Abstract #2319. [12] Sutter B. et al. (2009) *New Martian Chemistry Workshop*, Abstract #8004. [13] Boynton W. V. et al. (2009) *Science*, 325, 61-64. [14] Sutter B. et al. (2009) *LPS XXXX* Abstract #1843.

## EXPERIMENTAL WEATHERING OF OLIVINE, MG-SIDERITE, AND OLIVINE-BASALT WITH SULFURIC ACID: IMPLICATIONS FOR THE FORMATION OF HEMATITE-ASSOCIATED

**SEDIMENTS IN MERIDIANI PLANUM, MARS.** A. M. Koster<sup>1</sup> and D. C. Golden<sup>2</sup> <sup>1</sup>Calvin College, 3201 Burton St. Grand Rapids, MI 49568 (amk35@students.calvin.edu) <sup>2</sup>ESCG Mail Code JE23 Houston, TX 77058 (d.c.golden@nasa.gov)

**Introduction:** In January of 2004 the Mars Exploration Rover Opportunity landed within Eagle crater on Meridiani Planum (MP), Mars [1]. MP was initially chosen as a suitable landing site for Opportunity due to the discovery of crystalline gray hematite [2,3], which is indicative of aqueous processes, and because of its suitability as a landing site [4]. After a brief stay in Eagle Crater, Opportunity moved on to Endurance Crater [1] where it encountered a suite of sedimentary rocks known collectively as the “Burns Formation” [1,5,6]. This group of sandstones contains sulfate rich evaporites, siliclastic material derived from olivine-basalts, and iron-rich concretions [1,7,5]. These nearly spherical iron-rich concretions, found in lag deposits and within the Burns Formation, consist mostly of hematite [1,7,8] and are of particular interest because of their possible implications for the aqueous history of MP. There are many hypotheses for the formation of these spherules. These include formation by aqueous, volcanic, or impact processes [7,9,10,11].

	Olivine (San Carlos)	Siderite (Londerry, Nova Scotia)	Basalt (Kona, Hawaii)
Oxide	Wt%		
<b>SiO<sub>2</sub></b>	40.26	0.50	45.77
<b>Al<sub>2</sub>O<sub>3</sub></b>	0.25	0.15	13.05
<b>Fe<sub>2</sub>O<sub>3</sub>T</b>	10.42	74.03	10.94
<b>MgO</b>	47.83	21.87	15.63
<b>CaO</b>	0.24	1.65	12.28
<b>Na<sub>2</sub>O</b>	0.10	0.08	1.23
<b>K<sub>2</sub>O</b>	0.01	0.03	0.02
<b>Total</b>	99.57	99.93	100.11

**Table 1.** Major element concentrations in the rocks and minerals used for the hydrothermal reactions.

Evidence points to aqueous processes such as: the breakdown of iron rich sulfates (e.g. jarosite) through interaction with chemically distinct groundwater [12,13,14,7,1] or the oxidation of pyrite-rich deposits formed by the release of sulfide-rich hydrothermal water [9,12] as mechanism for spherule formation. These processes would have taken place during the late Noachian or early Hesperian epochs [7]. Several studies have been performed to understand the formation of Meridiani-like sediments. These studies have shown that there is a very specific set of conditions under

which they can form (e.g. 12). We postulate that these spherules and the sedimentary rocks in which they formed are a result of the weathering of primary basaltic materials and secondary iron bearing minerals under acidic hydrothermal conditions. Our objective here is to extend the spherule formation studies done by Golden et al. (2008), to include Mars-like parent materials i.e. olivine, Ca-Mg-Fe-carbonate, and olivine-basalt.

Treatment#	Wt of mineral/rock (g)	0.5M H <sub>2</sub> SO <sub>4</sub> (mL)	Rock/Acid g/g
0	0	10	0
1	0.1	10	0.01
2	0.25	10	0.025
3	0.5	10	0.05
4	1.00	10	0.1
5	2.50	10	0.25
6	5.00	10	0.5

**Table 2.** The Experimental treatments used in the hydrothermal reactions. The weight of the mineral or rock is increased while the amounts of sulfuric acid and sodium perchlorate (not shown) remain constant through all treatments.

**Materials and Methods:** San Carlos Forsterite (Fo90Fa10); a siderite sample from Wards Natural Science, NY consisting mainly of magnesite and ankerite; and an olivine-basalt sample from Kona, Hawaii were ground under acetone (<75µm) and air dried. The composition of the samples is given in Table 1. These samples were used as starting materials for the hydrothermal experiments at six rock/acid ratios (Table 2). The mixtures were placed in a 25-mL Teflon-lined, stainless steel vessel (Parr Instrument Co.) with the oxidant sodium perchlorate, closed tightly, and placed in an oven at 150C for 22.5 hours. At the end of the experimental run, the vessels were cooled back to room temperature, pH recorded, and the solid residues were washed with Milli-Q water and freeze-dried. The supernatant was freeze-dried separately. The residual mineral phases and the freeze-dried supernatants were analyzed by X-Ray diffraction, scanning electron microscopy (SEM), and transmission electron microscopy (TEM). For treatments 4-6 of the olivine experiment (Table 2), the supernatants were decanted after recording the pH and freeze-dried. The solids portion was present as two sedimentary layers: a lower layer of

mostly unaltered olivine, and an upper gelatinous layer containing gray or red particles. These two layers were harvested separately, and freeze-dried. Fractions of the freeze-dried precipitates were washed and freeze-dried again to obtain mineralogy of the water insoluble residue. Quantitative phase analysis of hydrothermal reaction products was performed by using HighScore Plus software on X-Ray Diffraction patterns obtained using a Panalytical X'pert Pro instrument operating at 45 kV and 40 mA using Cu-K $\alpha$  radiation. Rietveld refinement, a full pattern fitting method, was used to quantitatively define the reaction products.

**Results:** The morphology and chemistry of the starting materials and the products were obtained using electron beam methods (Figure 1) and quantitative data gained from the Reitveld Refinements of the products of the hydrothermal reactions versus the rock/acid ratio (R/A) are given in Figure 2.

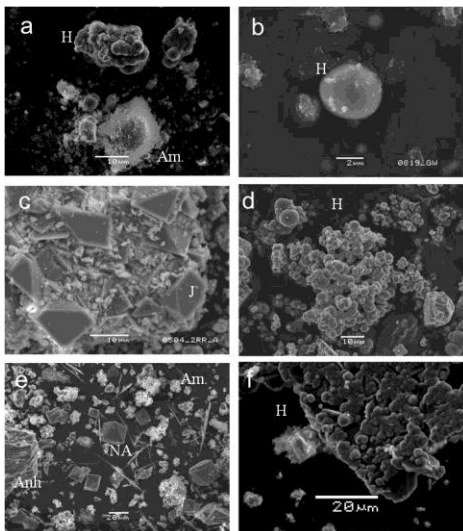


**Figure 1.** SEM images of the products of the hydrothermal reactions of olivine (a. and b.), siderite (c. and d.), and olivine-basalt (e. and f.). H: hematite spherules, Am: amorphous silica, J: jarosite, NA: natroalunite, and Anh: anhydrite.

*The Olivine Experiment:* pH in the olivine experiment increases rapidly at first, with increasing R/A ratio, but as the R/A ratio increases, the pH tends to get buffered. All treatments contain amounts of amorphous silica in the residue the fraction of which decreases as pH increases. Residual olivine is first seen at an R/A of 0.05 and increases with increasing R/A. Hematite spherules formed in treatments where the R/A is between 0.025 and 0.2. Hematite found in high R/A ratios were red and did not form spherules. The amount of hematite formed is greater in the treatments where the R/A and pH are low (Fig. 2a) but not extremely acidic (pH<0.7). In treatments where R/A>0.1, minor amounts of goethite were also detected. The soluble

components of these reactions consisted of magnesium sulfates and iron when the pH was <0.7.

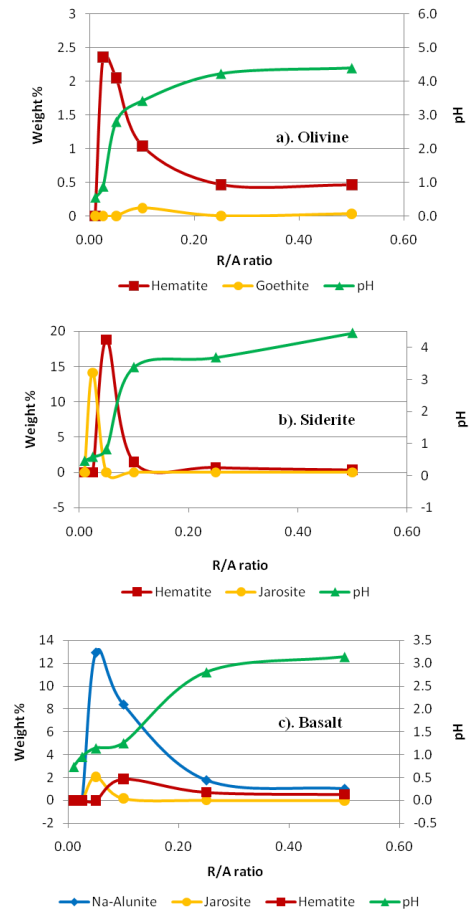


**Figure 2:** Graphs of the pH and the weight percents of the Fe and S bearing products of the hydrothermal experiments as a function of rock to acid ratio. Graph a. is for olivine, b. for siderite, and c. for olivine-basalt.

*The Siderite Experiment:* As in the olivine experiment, pH initially increases rapidly with R/A and then gets buffered at high R/A values. No amorphous component was detected in this siderite – H<sub>2</sub>SO<sub>4</sub> experiments because there were no silicate minerals as those found in olivine and olivine basalt. The first treatment (R/A 0.01) produced only soluble products. The second treatment produced an insoluble residue of jarosite, seen as cubic crystals in SEM images. Hematite was detected as being the dominant phase in the third treatment (R/A 0.05) and decreased in amount with increasing R/A ratio (Fig. 2b) as does jarosite, but the curve was shifted more towards higher R/A ratios. SEM confirmed the presence of spherules in the third treatment. Higher R/A ratio products contained increasing amounts of unreacted carbonate along with minor anhydrite. In treatment five (R/A=0.25) a minor amount of magnesioferrite was detected.

*The Olivine-Basalt Experiment:* As in the two previous experiments, pH increased rapidly with increasing R/A and leveled out in later treatments due to buffering, but the final pH of the highest R/A treatment was 3.2 in contrast to about 4.4 in corresponding R/A ratio of olivine and siderite experiments. Unreacted olivine-basalt was found in the residue for R/A > 0.05. Na-Alunite, jarosite, and hematite were also found in the residue (Fig. 2c) as precipitated products in the R/A range 0.05 to 0.25. The presence of Na-Alunite is attributed to the aluminum content of the basalt. Na-Alunite and jarosite both increase rapidly with R/A and then decrease. The amount of hematite also increases rapidly with R/A, but only after jarosite has begun to decrease in amount. SEM images show clumps of hematite spherules present in the residue where hematite formation is at its maximum. Amorphous silica is present in the residue and decreases slightly with increasing R/A. Calcium sulfates are found in samples where R/A was between 0.025 and 0.05.

**Discussion:** The experiments described above demonstrate the formation conditions for hematite spherules as a function of R/A ratio, pH, and compositions of the initial reacting materials. These results indicate that hematite formation occurs under very specific conditions. Data gathered about R/A ratio from the experiments indicates that hematite spherules are formed in hydrothermal reactions between R/A ratios of 0.05 to 0.1 (F/R ratios of 20-10). The stability diagram for the formation of hematite under acid sulfate conditions has been modeled using the Geochemist's Workbench software as functions of Eh and pH (figure 3). The stability fields of phases of interest are demarcated on this diagram. Reactions are indicated by the arrows which cross these boundaries. In these reactions precursor material (e.g. olivine, siderite) is broken down by sulfuric acid to form ferrous sulfates with a pH decrease. Ferrous sulfate is then oxidized to form ferric sulfate by the oxidant  $\text{NaClO}_4$ . Ferric sulfate hydrolyzes with increasing pH and forms jarosite. As pH continues to increase, jarosite undergoes hydrolysis and polymerization, forming hematite as a stable end product. These reactions are marked on the Eh-pH diagram for olivine (figure 3). A similar diagram can be drawn for siderite. The siderite reactions agree closely to those of olivine making it possible for hematite to form from siderite in a similar manner to olivine. For more complex basalt sulfuric acid reactions, the same process applies for iron bearing minerals; however there are other sulfates which precipitate along with iron sulfates and hematite (e.g. alunite anhydrite). The ferric sulfate-jarosite-hematite association observed in these reactions is similar to what is found at MP. The dashed box in figure 3 represents the possible Eh-pH conditions (Eh ~ 0.75-1.5V, pH ~ 1-2.5) which

could have been present at MP during the time when the spherules formed.

**Conclusions:** If sulfuric acid weathering was a dominant formation process at MP, then the following conditions may have been prevalent: Eh ~ .75–1.5V and pH ~ 1-2.5 at fluid to rock ratios of >0.05 (Rock/Acid < 20). Furthermore, the close agreement between the olivine and siderite reactions indicates that these conditions may have prevailed regardless of the nature of the starting rock.

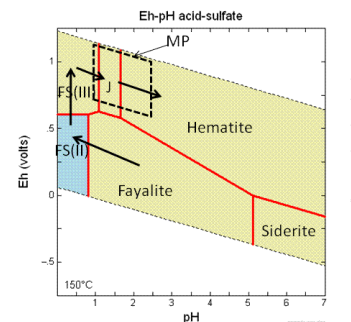


**Figure 3.** The stability diagram for the formation of hematite under acid sulfate conditions as a function of Eh and pH. The stability fields for the phases are demarcated on the diagram. The arrows represent a chemical reaction. The dashed box represents the mineral association found at Meridiani Planum and the Eh/pH conditions. FS(II) is ferrous sulfate, FS(III) is ferric sulfate.

**Acknowledgements:** We would like to thank the LPI and NASA's ARES directorate as well as the Mars Geochemistry Group. Specifically we would like to thank Brad Sutter and Cherie Achilles for their assistance with XRD and SEM.

**References:** [1] Squyres S.W. and Knoll A.H., (2005) *EPSL*, 240, 1-10. [2] Christensen, P.R. et al., (2000) *JGR*, 105, 9623-9642. [3] Christensen, P.R. et al., (2001) *JGR*, 106, 23,823-23,871. [4] Golombek, M.P., et al., (2003) *JGR*, 108, 8072, doi:10.1029/2003JE002074. [5] Grotzinger, J.P. et al., (2005) *EPSL*, 240, 11-72. [6] Arvidson R.E. et al., (2005) *JGR*, 111, E12S08, doi:10.1029/2006JE002728. [7] McLennan, S.M. et al., (2005) *EPSL*, 240, 95-121. [8] Morris, R.V., et al., (2005) *EPSL*, 240, 168-178. [9] Zolotov, M.Y. and Shock, E.L. (2005) *GRL*, 32, L21203, doi:1029/2005GL024253. [10] McCollom, T.M. and Hynke, B.M., (2005) *Nature*, 438, 1129-1131. [11] Knauth, L.P. et al., (2005) *Nature*, 438, doi:10.1038/nature04383, 1123-1128. [12] Golden D.C. et al., (2008) *American Mineralogist*, 93, 1201-1214. [13] Tosca N.J. et al., (2005) *EPSL*, 240, 122-148. [14] Barron V. et al., (2006) *EPSL*, 251, 380-385.

**EXPERIMENTAL EVOLUTION OF YAMATO 980459 VIA EQUILIBRIUM CRYSTALLIZATION AT 0.5 GPa: APPROACHING QUEEN ALEXANDRA RANGE 94201?** Cameron M. Mercer<sup>1</sup>, John H. Jones<sup>2</sup>, David S. Draper<sup>2</sup>, Tomohiro Usui<sup>2</sup>, and Loan H. Le<sup>3</sup>, <sup>1</sup>Middlebury College, 3737 Middlebury College, Middlebury, VT 05753 (cmercer@middlebury.edu), <sup>2</sup>Mail Code KR, NASA, Johnson Space Center, 2101 NASA Road 1, Houston, TX 77058, <sup>3</sup>Jacobs Sverdrup Co., Houston, TX 77058.

**Introduction:** The Martian meteorite Yamato 980459 (hereinafter Y98) is an olivine-phyric shergottite, with large olivine megacrysts set in a groundmass of finer grained olivine, pyroxene, chromite, and glassy mesostasis; plagioclase is not present [1]. Thin sections of Y98 yield modal proportions of major minerals in the ranges 8.7–26 vol% olivine, 48–52.6 vol% pyroxene, and 25–37 vol% mesostasis [1, 2, 3, 4]. Y98 is widely considered to be one of the most primitive shergottites ( $Mg\# = \text{molar } [Mg]/[Mg + Fe] = \sim 65$ ) [1, 4, 5, 6, 7], along with the new Martian meteorite North West Africa 5789 (NWA 5789), an olivine-phyric shergottite found in early 2009 that is remarkably similar to Y98 [8]. While Y98 was initially regarded as a primary melt composition derived from a reduced source in the Martian mantle (e.g. [4, 5]), Usui et al. [1] argue that the olivine megacrysts in Y98 are cumulus grains that crystallized in more reducing conditions than the groundmass olivines. However, Usui et al. also demonstrate in detail that the megacryst cores are in chemical equilibrium with Y98 whole-rock composition, and conclude that it may still be used as a Martian primary melt in experimental studies.

Another Martian meteorite, Queen Alexandra Range 94201 (QUE), has a coarse igneous texture and is classified as a basaltic shergottite composed mostly of clinopyroxene, maskelynitized plagioclase, and *no* olivine. Modal mineral abundances are 42–43.8 vol% clinopyroxene, 43–46 vol% maskelynite, 3.9–6 vol% merrillite, 2–4 vol% opaques, and 4–5 vol% mesostasis [9, 10]. QUE is most likely an evolved, i.e. differentiated, basalt with  $Mg\# = \sim 36$  [11], and incompatible element abundances exhibiting a strong depletion in LREEs [9]. In addition, QUE is also considered a true Martian liquid composition [7, 9, 12], and some of its isotopic and trace element compositions are shared with Y98 [7].

Since Y98 and QUE are thought to represent genuine liquid compositions, and because of their similarities in isotopic and trace element compositions, it is important to explore possible petrogenetic relationships between them. Previous work to this end includes MELTS petrological modelling to demonstrate that a Y98 parent composition could reproduce many of the characteristics of QUE via fractional crystallization [13]. In addition, experiments at 1 bar by Galenas et al. [14], and at 0.5 GPa by Draper [7] have been conducted to simulate this process by equilibrium crystallization. Galenas et al. [14] produced QUE-like liquids from a Y98 starting composition that were similar to QUE in major element abundances, but not in minor element abundances. They suggest that a Y98-like source region that had undergone less partial melting than Y98 could potentially produce a QUE parent magma after fractional crystallization. The initial results from Draper's anhydrous equilibrium experiments are promising, though not yet conclusive, that a QUE-like composition may be produced

by Y98 parent materials. We have conducted additional experiments designed to extend the work done by Draper in an effort to evaluate whether or not Y98-like materials can generate residual melts of QUE composition by equilibrium crystallization.

**Experimental and Analytical Methodology:** Experiments were conducted in a Quickpress piston cylinder apparatus at NASA's Johnson Space Center (JSC) using BaCO<sub>3</sub> assemblies, MgO spacers, and graphite furnaces and sample capsules. Note that Draper [7] used talc-pyrex cells rather than BaCO<sub>3</sub>, potentially affecting the comparison of results between the two sets of experiments. The oxygen fugacity of each experiment was  $\sim QFM-1.5$  based on experimental measurements by Righter et al. [15].

Starting material was a synthetic glass powder of Y98 composition prepared following standard procedures at JSC. Oxide and carbonate compounds were initially dehydrated and weighed out into the desired proportions before being mixed and ground under acetone. They were then dried, placed in a Au-Pt alloy crucible, and melted at temperatures between 1300–1500°C for  $\sim 4$  hours. Finally, the material was water quenched, reground, and dried. The powder used in this study is the same starting material used previously by [5, 7, 14, 16].

Loaded assemblies were placed in the piston cylinder and initially overpressurized to  $\sim 130\%$  of the final run pressure. The pressure was then allowed to fall to 0.5 GPa while the temperature was ramped up over a 30 minute period. Each experiment was initially held at a temperature of 1500°C (well above the liquidus for Y98 at 0.5 GPa, [6]) for  $\sim 30$  minutes before ramping down to the run temperature. Ramp-down durations were 13–30 minutes long. Final temperatures ranged from 1150–1300°C, and are listed along with the run durations for each experiment in Table 1. Charges were quenched isobarically by cutting power to the apparatus while maintaining piston pressure, allowing the temperature to fall to ambient in  $\sim 1$  minute. Run products were mounted in epoxy, cut, and polished to 0.25  $\mu m$  for analysis.

The JEOL JSM-5910LV scanning electron microscope (SEM) at JSC was used to acquire backscattered electron (BSE) images of each experimental charge, and to perform qualitative identification of melt and crystalline phases using an energy dispersive X-ray spectrometer. JSC's Cameca SX100 electron probe microanalyser (EPMA) was used to determine the composition of silicate minerals and residual melt. Operating conditions were: 15 kV accelerating voltage, 20 nA beam current, 1  $\mu m$  focused electron beam (for crystalline phases), and peak and background counting times of 20–40 s per element. For glass analyses a 5  $\mu m$  raster was used to minimize loss of volatile elements. Analytical standards were well-characterized synthetic oxides and minerals, and quality of data was insured by analyzing the standards as

Table 1: Run temperatures, durations, and product descriptions. Abbreviations: ol = olivine; pyx = pyroxene; plag = plagioclase; ulv = ulvöspinel; chr = chromite.

Sample	$T$ (°C)	Duration (h)	Mineral Assemblage*
CM-01	1200	3	ol, pyx, glass
CM-02	1150	3	ol, pyx, plag, little glass
CM-03†	1250	3	ol, pyx, plag, glass
CM-04	1300	3	ol, pyx, glass
CM-05	1275	3	ol, pyx, glass
CM-06	1300	24	ol, pyx, glass, minor chr
CM-07†	1250	24	ol, pyx, plag, glass, minor chr
CM-08§	1150	61	ol, pyx, plag, minor ulv
CM-09	1200	54	ol, pyx, glass

\* All charges had Fe-metal blebs present.

† Plagioclase preferentially near bottom of charge.

§ Charge near the solidus; modal mass balance likely erroneous.

unknowns. Mineral and glass compositions were used to calculate the modal proportions of all phases using least-squares mass-balance. With the exception of sample CM-02, all modal calculations gave  $r^2$  values of  $<0.43$  (where  $r^2$  is the sum of the square of the residuals). To test whether equilibrium was achieved, the Fe-Mg exchange coefficient between olivine and the residual liquid,  $K_D = [\text{Fe}/\text{Mg}]_{\text{olivine}}/[\text{Fe}/\text{Mg}]_{\text{glass}}$ , was calculated for each charge that had a glass phase.

**Experimental Results:** Experiments at or above 1275°C yielded charges composed of olivine, low-Ca pyroxene, and glass (quenched melt). At 1250°C, plagioclase also entered the assemblage. In both 1250°C run products the plagioclase was clustered in the lower portion of the charge. Minor amounts of chromite was present in the 54 hour run at 1200°C, with grain sizes  $\leq 20\mu\text{m}$ . Both 1200°C experiments were composed solely of olivine, pyroxene, and glass; plagioclase was *not* present in either charge. However, plagioclase was again present in both 1150°C runs, along with olivine, pyroxene, and glass.

The longer duration ( $\sim 61$  hour) 1150°C charge also had minor amounts of (barely) analyzable ulvöspinel, and rare un-analyzable phosphate grains in the interstices. Both low-temperature experiments had small interstitial pockets of pure  $\text{SiO}_2$ . Table 1 summarizes the major mineral phases present in each sample. All run products had small amounts of Fe-metal present, typically located along the bottom of the charge.

Figure 1 shows a typical run product. Chemical zoning of olivine and pyroxene occurs to greater or lesser degrees in all run products (Figure 2). Typically olivine cores are more magnesian than the rims. For example, in CM-06B, the most magnesian core analyzed has  $\text{Fo}_{81}$  while the most ferroan rim has  $\text{Fo}_{44}$ . Zoned pyroxenes usually have cores of pigeonite and rims of augite (Figure 2b–2c). In most cases, distinct core and rim compositions could be identified for olivines and pyroxenes. Sometimes a distinct mantle composition (intermediate between the core and rim) could also be identified. Most of the calculated olivine-liquid  $K_D$  values are not within the expected range of 0.31–0.34 [1]. The exceptions are: an olivine rim composition in CM-03A ( $K_D = 0.32$ ); and an olivine mantle composition in CM-04A ( $K_D = 0.31$ ). The composition of glass for these two charges were plotted versus their Mg#s along with previous data from Draper [7] (Figure 3).

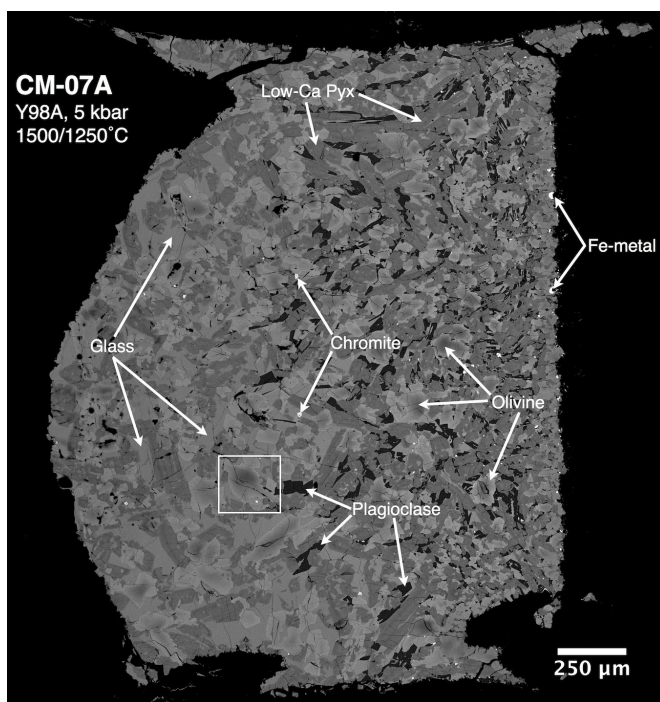
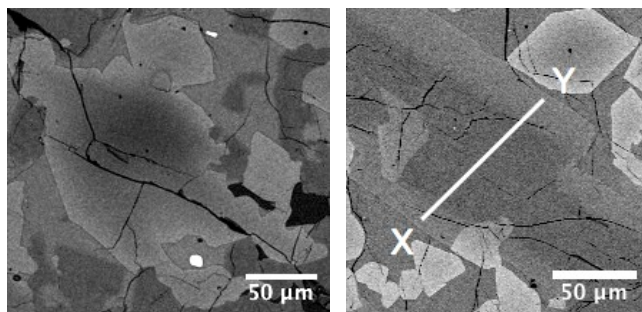
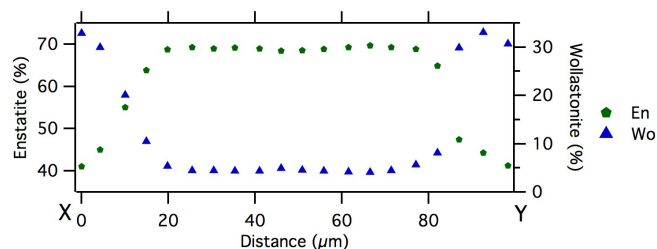


Figure 1: BSE image of sample CM-07A (15% glass, 19% olivine, 57% low-Ca pyroxene, 8% plagioclase, 0.4% chromite, and 0.6% Fe-metal). The black region around the charge is graphite. Note that plagioclase appears only on the bottom half of the charge (bottom to the right). The boxed olivine is visible in Figure 2a.



(a) A zoned olivine crystal in CM-07A, (b) A zoned pyroxene from CM-06B. Line is an EPMA analysis.



(c) Zoning profile in pyroxene from the line analysis in Figure 2b. The core is  $\text{En}_{69}\text{Fs}_{26}\text{Wo}_5$ , and the outermost rim reaches  $\text{En}_{43}\text{Fs}_{24}\text{Wo}_{33}$ .

Figure 2: Examples of chemical zoning in olivine and pyroxene.

**Discussion** The ubiquitous zoning in these experiments serves as an indicator that equilibrium conditions were not achieved. Samples CM-01 and CM-02 were so badly zoned that they only received a cursory examination with the EPMA; CM-05 was not examined at all. CM-03 and CM-04 were analyzed in the hopes that, because they were higher temperature runs, they would have more closely approached equi-

librium. However, while CM-03 and CM-04 did have  $K_D$  values close to the expected range (0.32 and 0.31, respectively) for the outer portions of olivine versus melt, they did not achieve equilibrium. This is reflected in their lower-than-expected Mg#s (Figure 3) because Fe did not have a chance to fully diffuse to the centers of the olivines, leaving a higher concentration in the glass.

It was initially thought that longer duration experiments would allow equilibrium conditions to be more closely approximated. In addition, we originally thought that the absence of plagioclase in CM-01 was due to our allowing insufficient time for plagioclase to nucleate, and that longer experiments would also help. Unfortunately, the longer duration experiments did not solve either of these issues, and in fact emphasized three of our conundrums.

First, in both 1250°C charges, plagioclase accumulated in the bottom portion of the charge (Figure 1). We interpret this to be an expression of a thermal gradient within the piston cylinder. The pertinent effect of this is that glass compositions in the bottom of the charge are slightly depleted in aluminum relative to glass in the upper region. For our purposes this was of little consequence.

Second, plagioclase failed once again to appear in the 1200°C run, despite it being present in both higher and lower temperature runs of short and extended durations. This may be due to experimental error, or could indicate that the crystallization of plagioclase is being suppressed somehow at 1200°C.

Third, CM-08 once again exhibited pockets of pure SiO<sub>2</sub> (similar to CM-02), which cannot be in equilibrium with olivine under the conditions of our experiment. This is most likely an expression of local disequilibrium conditions within the samples, further indicating that the experiments failed to reach equilibrium. This failure begs a review of our experimental methods. It is a virtual certainty that our ramp-down times were too long, thereby allowing at least Fo to crystallize at higher temperatures than desired.

A final and important consideration stems from the observation that CM-08 was effectively on or very near the solidus for this composition. If, as the temperature decreases, a Y98 parent melt is to produce residual liquids like QUE after equilibrium crystallization, that liquid must by necessity be generated before all of the original material crystallizes. However, if the solidus for a Y98 composition is at a higher temperature than the liquidus of a QUE-like composition at a pressure of 0.5 GPa, it may not be possible to produce a QUE-like liquid at this pressure.

**Conclusions and future work:** While preliminary results still hold some promise, the difficulties experienced here have so far prevented any judgement of whether a Y98 parent melt can produce a QUE-like composition by equilibrium crystallization. However, with appropriate corrections to our experimental methodology, it is likely that these problems may be overcome. Future experiments with drastically reduced ramp-down times are planned, and will be underway shortly.

**Acknowledgments:** We thank Lisa Danielson, Kellye Pando, and Kevin Righter for their generous support in per-

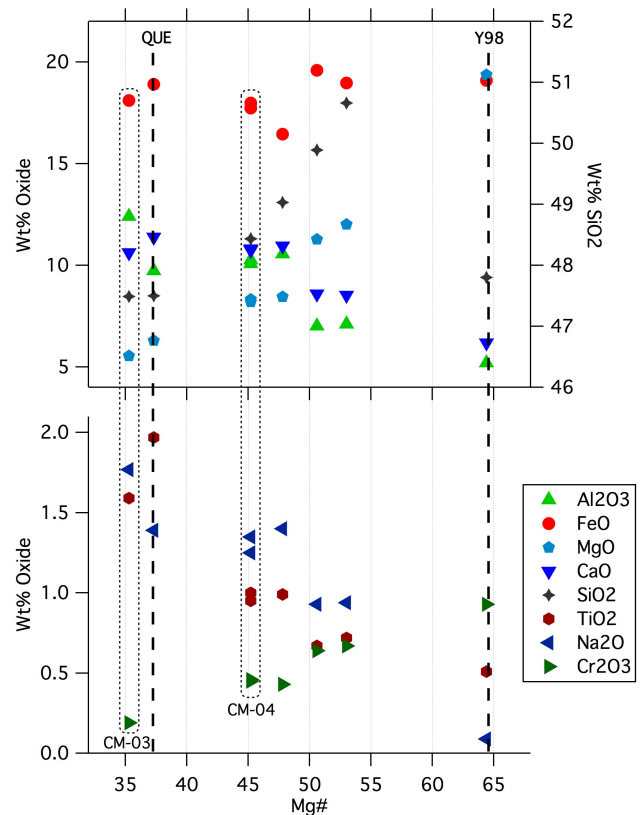


Figure 3: Compositions of liquids formed in CM-03 and CM-04 (circled) plotted with results by Draper [7]. Despite not achieving equilibrium, the new data plot roughly within the expected trends.

forming these experiments, as well as Georganne Robinson, Kent Ross, Cherie Achillies, and Anne Peslier for their aid in successfully acquiring SEM and EPMA analyses. We also thank Kathy Thomas-Keprta for her assistance in obtaining photomicrographs of our charges, and we greatly appreciate the insights and suggestions provided by Juliane Gross.

- References:** [1] Tomohiro Usui, Harry Y. McSween Jr., and Christine Floss. (2008). *Geochim. Cosmo. Ac.* 72(6). [2] Ansgar Greshake, Jörg Fritz, and Dieter Stöffler. (2004). *Geochim. Cosmo. Ac.* 10(68). [3] Yukio Ikeda. (2004). *Antarct. Met. Res.* 17. [4] Takashi Mikouchi and et al. (2004). *Antarct. Met. Res.* 17. [5] G. McKay and et al. (2004). *LPSC XXXV*, Abs. 2154. [6] Donald S. Musselwhite and et al. (2006). *Met. Planet. Sci.* 9(41). [7] D. S. Draper. (2009). *LPSC XL*, Abs. 1969. [8] Juliane Gross and et al. (In Review). *Met. Planet. Sci.* [9] Harry Y. McSween Jr. and et al. (1996). *Geochim. Cosmo. Ac.* 22(60). [10] Takashi Mikouchi, Masamichi Miyamoto, and Gordon A. McKay. (1998). *Met. Planet. Sci.* 33. [11] David W. Mittlefehldt and Marilyn M. Lindstrom. (1996). *LPSC XXVII*, 887–888. [12] David A. Kring and et al. (2003). *Met. Planet. Sci.* 12(38). [13] Steven J. K. Symes and et al. (2008). *Geochim. Cosmo. Ac.* 72. [14] M. G. Galenas, J. H. Jones, and L. R. Danielson. (2009). *LPSC XL*, Abs. 1920. [15] K. Righter, K. Pando, and L. R. Danielson. (2009). *Earth Planet. Sci. Lett.* 288. [16] Koizumi E. and et al. (2004). *LPSC XXXV*.

## In Search of Rayed Impact Craters for Insight into the Recent History of Saturn's Icy Moons.

Sean W. Murphy<sup>1</sup> and Paul M. Schenk<sup>2</sup>, <sup>1</sup>Lafayette College Department of Geology and Environmental Geosciences, 116 Van Wickle Hall, South College Drive, Easton, PA 18042 ([murphys@lafayette.edu](mailto:murphys@lafayette.edu)), <sup>2</sup>Lunar and Planetary Institute, 3600 Bay Area Boulevard, Houston, TX 77058 ([schenk@lpi.usra.edu](mailto:schenk@lpi.usra.edu)).

**Introduction:** Crater density and distribution statistics have long served as a means to characterize and age-date surfaces of asteroids, planets, and moons. Recent mapping of Saturn's icy satellites reveals complex geologic histories on those bodies [1]. By analyzing the characteristics and distribution of the youngest of these craters on Saturn's icy moons, so called 'rayed craters,' light may be shed on processes currently active within the Saturnian system. Specifically, we hope to gain insight into the nature of the current impacting population, as well as other processes that have dominated surface alteration on the inner icy satellites of Saturn in recent times.

Of primary concern to our study is identifying the current impactor population. Two main populations have been proposed (we ignore asteroids as these are not dynamically important under current conditions). For a moon orbiting one of the large outer planets, Zahnle et al. [2] confirmed, both with simulations and observations, that cratering rates by a heliocentric population should be much greater on the leading hemisphere than the trailing, though their observed density was much lower than that predicted by models. Conversely, models show that a planetocentric population (likely dominated by secondary projectiles launched into Saturn orbit) will produce a weak 1:2 global cratering asymmetry favoring the hemisphere opposite that of the original source basin [3].

In addition, Schenk et al. [4] document prominent global color pattern similarities between many of the icy satellites of Saturn. These patterns include an enhancement in redness in the infrared at both the apex and antapex on Dione, Rhea, and Tethys. The increased redness surrounding the apex was attributed to E-ring deposition, while that at the antapex could be the result of plasma bombardment. The study also found equatorial blue bands on both Tethys and Mimas, which they attributed to incident MeV electrons that flow in a direction opposite that of the plasma. Our goal is to explain how these factors, in addition to impacts themselves, have affected the surfaces of Saturn's moons in the geologically recent past up to the present.

**Methods:** Mosaics have been produced by P. Schenk from the *Cassini* ISS Narrow Angle Camera. These global mosaics cover the surfaces of Dione, Rhea, and Tethys at resolutions of ~1 km/pixel (Figure 1). Mosaics that cover 15 to 75% of these surfaces reach resolutions of 100-750 m/pixel. Still higher resolution

images, with very limited spatial coverage, are on the scale of 50-80 m/pixel. All maps are in 3 colors: Infrared (IR; 0.930  $\mu\text{m}$ ), Green (GRN; 0.568  $\mu\text{m}$ ), and Ultraviolet (UV; 0.338  $\mu\text{m}$ ), with the exception of the highest resolution mosaics for Rhea which use the IR1 (0.752  $\mu\text{m}$ ) filter. Color ratio maps were also used to make relative color recognition more accessible. For instance, the color ratio map IR/UV shows the relative redness of a surface as compared to blueness. The other color ratio maps available are Gr/UV and IR/Gr.



**Figure 1.** Three-color global map of Dione. Map is in simple cylindrical projection. Longitude goes from 360°W to -2°W, left to right.

Using all 4 maps available for a given image sequence (the 3-color composite and 3 ratio maps) we searched for rayed craters on global maps of Dione, Rhea, and Tethys, with somewhat more limited data available for Iapetus. The basic criterion for a "rayed" crater is one that has an ejecta deposit consisting of relatively bright material or material of a distinctly different color radiating from its center and extending beyond the rim, like spokes on a wheel (Figure 2). Rayed craters could show a color signature in any combination of ratio images, as long as it was recognizable in at least two mapping products.

Data recorded and/or calculated for each rayed crater includes: latitude, longitude, distance from apex, diameter, albedo, and the basic color characteristics of the deposit. The last criterion is defined by how distinctive the ray deposit is in any one or two of the three image filters, and is defined by comparison with surrounding terrain. For instance, in the IR/UV ratio map, rays could be bright (red), dark (blue), or neither (neutral). Rays can also be bright generally yet display no color differences (i.e., a neutral color).

The final product of our survey of Dione, Rhea, and Tethys is a catalog of rayed craters found in medium resolution (>0.75km/pixel) images and rayed craters found only in high resolution (<0.75km/pixel) images.

A global distribution map of the rayed craters was produced for each moon (e.g., Figure 3), distinguished by whether craters were found in high or medium resolution images. Next, we plotted a size-distribution map of rayed craters on each moon. For Dione and Rhea, size groups of craters are: those that have diameters <3 km, those between 3 and 10 km, and those with diameters >10 km. Because we found no rayed craters greater than 10 km in diameter on Tethys, the only cutoff is at 3 km diameter.

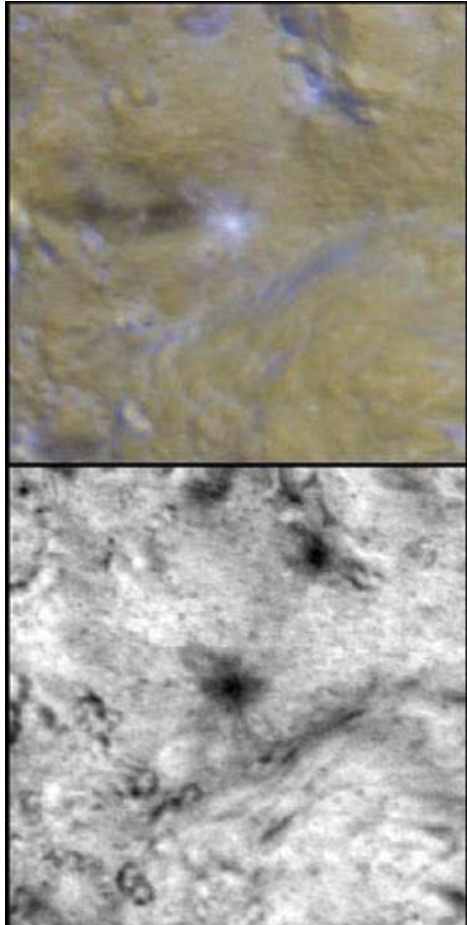


**Figure 2.** Rayed crater shown in 3-color image (top) and in IR/UV ratio image map (bottom). Crater diameter: ~0.42 km.

**Results:** Our global ray distribution maps show similarities and differences between the three moons. In Dione medium resolution imaging, 40 out of 50 (~4:1) rayed craters were found on the leading hemisphere. On Rhea, 12 out of 18 (~2:1) were found on the leading hemisphere, while Tethys has 12 out of 15 (~4:1) on its leading hemisphere. Given the possibility that one or two rayed craters could have been overlooked, our findings are consistent with a 3:1 to 4:1 leading to trailing hemisphere cratering rate asymmetry, similar to that found on Ganymede by

Zahnle et al [2]. Although our high resolution maps do show many very small rayed craters (<0.5 km diameter), they were ignored here because of the limited spatial sampling.

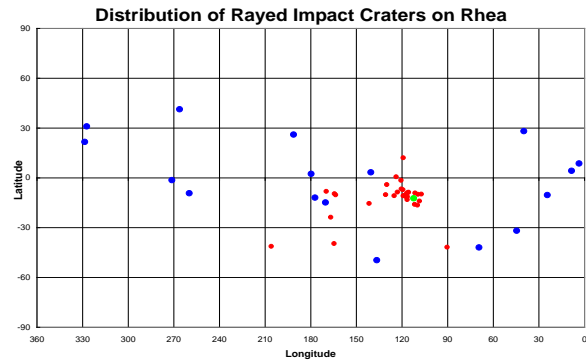


**Figure 3.** Global distribution map of rayed craters on Rhea. Craters found in medium resolution images are in blue, those found only in high resolution images are in red. *Inktomi* (Diameter: ~48km) is in green.

While there are several color “types” among the rays identified, two types are especially common on these moons. On Dione, nearly twice as many ‘RG’ craters (red in the IR/UV, green in the Gr/UV) were found as ‘BB’ craters (blue in both the IR/UV and Gr/UV). This is in contrast to Rhea, on which there were ~7 times as many ‘BB’ craters found as ‘RG’. Tethys has about twice as many ‘BB’ as ‘RG’ craters, but also shows other types with comparable numbers. Lastly, We present 3-point spectrum line plots which show relative intensity of rays and the background terrains on which rays were found, in all 3 color bands (e.g., Figure 4).

**Discussion:** Concentrations on the leading hemispheres of these moons are consistent with those predicted for a planetocentric population by Alverellos et al. [3]. However, no prominent source craters or basins have been identified on the opposing (i.e., trailing) hemispheres. Likely relatively young source craters (*Creusa* on Dione and *Inktomi* on Rhea) are on the same hemisphere as the highest concentration of putative return secondary impactors, contrary to the expectation of Alverellos et al. [3].

Heliocentric impactors are expected to produce a much higher concentration of craters on the leading hemispheres of synchronous satellites [2]. The weak asymmetries we observe would seem to be inconsistent with this model. One mechanism to reduce the expected asymmetry to the observed asymmetry would be to “depopulate” the leading hemisphere by another process. In this case, E-ring dust deposition is a likely cause of rapid ray erasure. Because the relative rates of surface alteration on the trailing and leading

hemispheres are unknown, differential ray erasure, if it occurs, would make crater ray distribution unusable for identifying source populations. The fact that we observe relatively consistent asymmetries suggests that we are seeing a real effect, however.

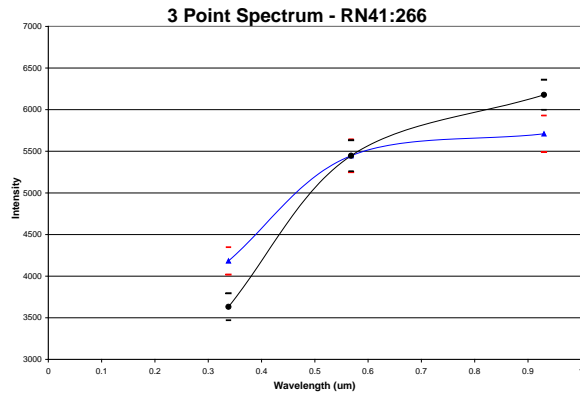


**Figure 4.** 3-point spectrum for a representative ‘BB’ rayed crater (~41°N, 266°W) on Rhea. The blue curve represents the ray deposit, while the black curve is that of local terrain surrounding this crater. Ray intensities have been normalized with respect to the green band of the terrain to eliminate albedo effects.

#### References:

- [1] Dougherty, M., L. Esposito, and S.M. Krimigis (2009). *Saturn from Cassini-Huygens*. Dordrecht, New York.
- [2] Zahnle, K. et al. (2001) *Icarus* 153, 111-129.
- [3] Alvarellos, J. et al. (2005) *Icarus* 178, 104-123.
- [4] Schenk, P. et al. (2010) *Icarus*, in press.

**IMPACT MELTS AND GRANULITES IN THE LUNAR METEORITE PCA 02007.** William M. Vaughan<sup>1</sup>, Axel Wittmann<sup>2,3</sup>, Katherine H. Joy<sup>2,3</sup>, and David A. Kring<sup>2,3</sup>. <sup>1</sup>Department of the Geophysical Sciences, University of Chicago, 5734 South Ellis Ave., Chicago, IL 60637, USA, [wvaughan@uchicago.edu](mailto:wvaughan@uchicago.edu), <sup>2</sup>Lunar and Planetary Institute, 3600 Bay Area Blvd., Houston, TX 77058, USA. <sup>3</sup>NASA Lunar Science Institute, [Wittmann@lpi.usra.edu](mailto:Wittmann@lpi.usra.edu); [Joy@lpi.usra.edu](mailto:Joy@lpi.usra.edu); [Kring@lpi.usra.edu](mailto:Kring@lpi.usra.edu)

**Introduction:** Hypervelocity impacts shape the surfaces of terrestrial planets and asteroids. The rocks produced by impacts record information about the collisional history of their parent solar system bodies.

We investigated the lunar meteorite Pecora Escarpment (PCA) 02007, a feldspathic regolith breccia [1-5], to better understand the impact history of the Moon. We performed petrographic and geochemical analyses of PCA 02007's impact melt and granulite clasts—fragments of rock produced by impacts—to determine their lunar provenance and reconstruct their formational setting.

**Samples and Methods:** Three doubly polished sections (one ~100  $\mu\text{m}$  thick, two 30  $\mu\text{m}$  thin) of PCA 02007,<sup>37</sup> were prepared. Clast components were characterized with a petrographic microscope and a JEOL scanning electron microscope. A Cameca SX100 electron microprobe was used to determine the mineral chemistry and bulk composition of impact melt clasts, granulite clasts, and metal particles from the thick section. Silicates were analyzed with a 15 kV, 15 nA beam of 1  $\mu\text{m}$  diameter. Bulk clast compositions were derived using the same analytical setup with a defocused 20  $\mu\text{m}$  diameter beam. An estimate of the bulk composition of the thick section was made from an average of 29 defocused beam analyses of the matrix and is presented in Table 1. Metals were analyzed with a 15 kV, 20 nA beam of 1  $\mu\text{m}$  diameter. The NIH software ImageJ [6] was used to measure the percent area of mineral phases from back-scattered electron images to determine mineral modes.

**Results: Petrography.** PCA 02007 is a feldspathic regolith breccia composed of mineral, glass, impact melt, and granulite clasts set in a very fine-grained clastic matrix [1]. Figure 1a shows a representative area of the sample; note the agglutinate (A) and the impact-derived glass bead (B), which represent regolith components. The clast population is dominated by impact melts, although several fragments of ferroan anorthosite and low-Ti basalt occur. Our study focuses on 15 impact-melt clasts and 4 granulite clasts from 100 to 500  $\mu\text{m}$  in diameter. These clasts are subdivided into four textural categories: granoblastic granulites, clast-free impact melts, clast-bearing impact melts, and clast-rich impact melts, following the criteria of [7].

Figure 1b shows a typical granoblastic granulite. Granulite clasts are composed of equidimensional plagioclase crystals enclosing rounded-to-sub-rounded olivine and pyroxene crystals; they may also contain iron-nickel metal, troilite, or ilmenite as accessory phases.

Impact melt clasts are composed of euhedral plagioclase crystal laths; glassy interstitial melt, occasionally containing small olivine crystals and immiscible iron-nickel metal and troilite; and olivine, pyroxene, plagioclase, and chromite clasts. The relative proportions of crystals, clasts, and melt vary between different categories of impact melts: clast-free impact melts contain less than 10 vol. % clasts, clast-bearing impact melts contain between 10 and 25 vol. % clasts, and clast-rich impact melts contain more than 25 vol. % clasts [7]. Figure 1c shows a clast-rich impact melt with a wide range of clast sizes but uniformly very fine-grained (<30  $\mu\text{m}$ ), almost cryptocrystalline, plagioclase crystals. Figure 1d shows a clast-free impact melt with fine-grained (30-300  $\mu\text{m}$ ), euhedral plagioclase crystal laths. In general, clast-rich impact melts have smaller plagioclase crystals.

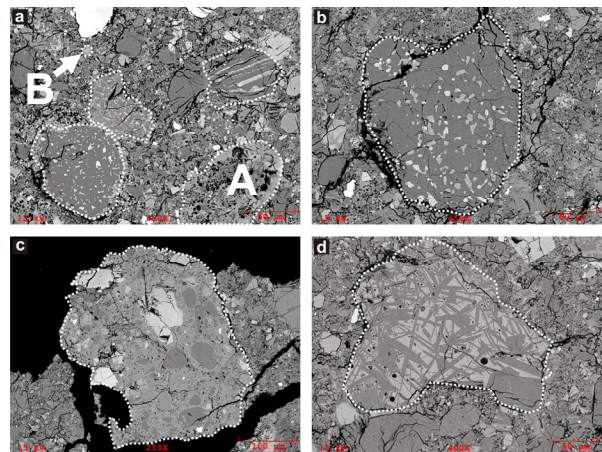


Figure 1. Back-scattered electron images of selected clasts from PCA 02007. (a) Overview of matrix showing agglutinate A at lower right, glass bead B at upper left, granoblastic granulite at lower left, and two clast-bearing impact melts. (b) Granoblastic granulite. (c) Clast-rich impact melt. (d) Clast-free impact melt. Plagioclase is dark gray; mafic phases are light gray. The glass slide and fractures appear black. Clasts are outlined with a dashed white line.

*Mineral chemistry.* We analyzed the mineral chemistry of 19 impact melt and granulite clasts in PCA 02007. All analyzed plagioclase is highly calcic ( $An_{92}$  to  $An_{98}$ , Fig. 2) with  $Or_{<0.4}$  and generally  $Or_{<0.1}$ . Plagioclase crystals that grew in impact melts cluster between  $An_{95}$  and  $An_{97}$ , whereas plagioclase clasts and plagioclase granulites are more variable—for example, they occupy the  $An_{92}$  and  $An_{98}$  extremes. Pyroxene and olivine clasts show more diversity in composition (Fig. 3). Pyroxene clast compositions are particularly diverse ( $En_{39-76}Wo_{1-37}Fs_{16-48}$ ). Olivine clast compositions are generally magnesian and range from  $Fo_{52}$  to  $Fo_{81}$ . Most olivine contains about 0.3 wt% CaO. Co/Ni ratios of the metal grains in PCA 02007 are similar to Co/Ni ratios of meteoritic metal [8], not ratios of metal found in Apollo rocks and soils (Fig. 4).

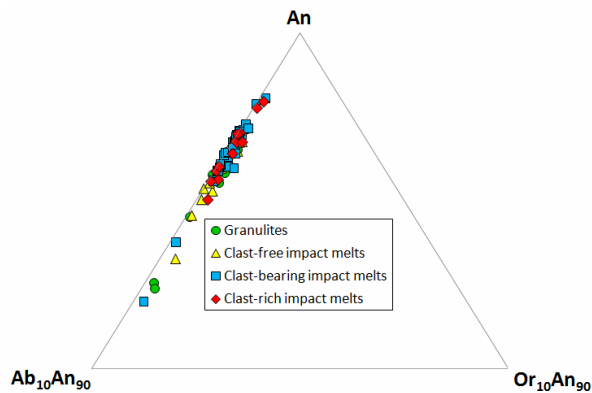


Figure 2. Composition of plagioclase in impact melt and granulite clasts from PCA 02007.

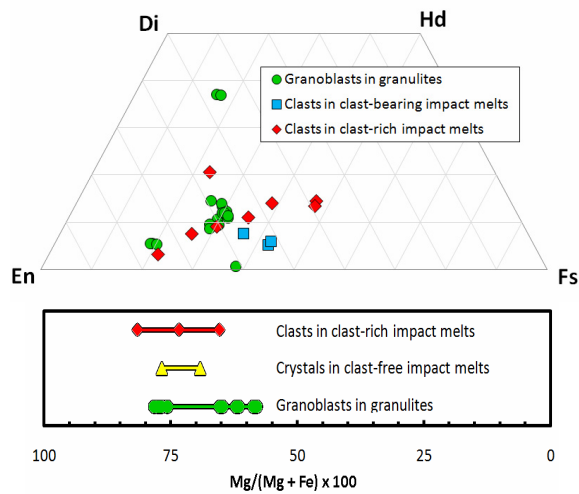


Figure 3. Composition of pyroxene (top) and olivine (bottom) in impact melt and granulite clasts from PCA 02007.

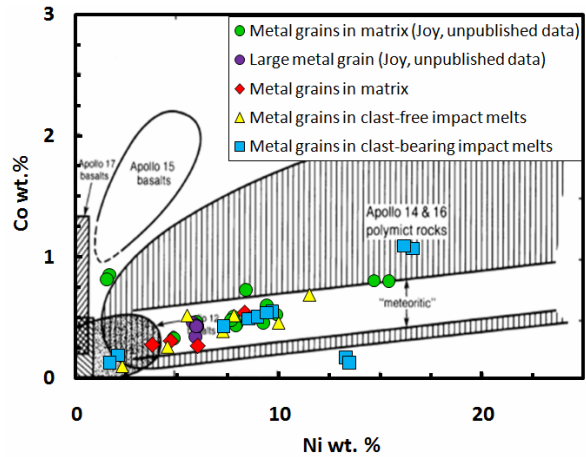


Figure 4. Composition of metal grains in PCA 02007 compared with compositions of metal grains from Apollo samples and meteoritic metal [8].

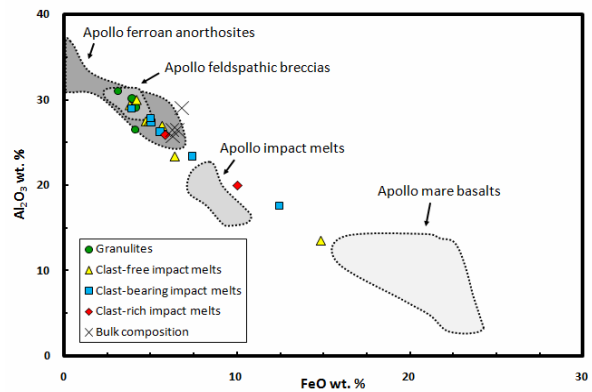


Figure 5. Bulk clast wt. %  $Al_2O_3$  vs. wt. % FeO compared with rock compositions from Apollo samples [9-11].

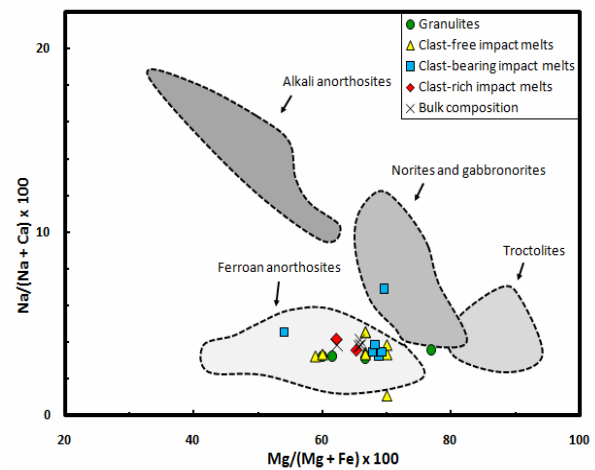


Figure 6. Bulk clast Na # vs. Mg # compared with highland rock suite (ferroan anorthosite, Mg-suite, and high-alkali-suite) compositions from Apollo samples [12].

**Discussion:** *Impact setting of impact melts and granulites.* Impactites sampled in PCA 02007 are products of several impact cratering processes: granulites are probably impact melts that have been buried and thermally metamorphosed by subsequently deposited ejecta blankets; they were therefore likely formed after energetic impact events that produced craters >30 km in diameter [13]. Impact melt-bearing fallback lithologies (clast-poor, clast-bearing, and clast-rich impact melts) likely come from proximal, near-surface ejecta deposits of impact craters [14]; glass beads could record contributions from more distal impact cratering events; and agglutinates record very small, local impact cratering events.

*Parent rocks of impact melts and granulites.* The bulk compositions of impact melt and granulite clasts record information about their parent target rocks. Figure 5 shows that the majority of impactite clasts in PCA 02007 are similar in composition to Apollo 16 feldspathic breccias, feldspathic melt breccias, and pristine ferroan anorthosites, indicating that their parent rocks were highly feldspathic. The bulk composition of PCA 02007 (Table 1, Fig. 5) is located at the Fe-rich end of the feldspathic lithology region, suggesting that PCA 02007 is a mix of highly feldspathic lithologies and more mafic material: see also [1] and [15]. PCA 02007 contains no significant KREEP component (no high-Na # rock types, Fig. 6: see also [1-5, 15]) so it may have been consolidated in a region of the moon unsampled by the Apollo and Luna missions.

Three impactite clasts are more mafic than feldspathic (Figs. 5 and 6). A Fe-rich (bulk 15 wt. % FeO) clast-free impact melt with a low Na concentration (0.06 wt. % Na<sub>2</sub>O) has high Ti (>0.5 wt. % TiO<sub>2</sub>), suggesting it was derived from mixing feldspathic and mare basalt lithologies. Two clasts have a Mg-suite affinity: a clast-bearing impact melt with a composition similar to Apollo norite/gabbronite (Fig. 6) and a magnesian granulite (Fig. 6). Trace element studies will constrain the provenance of this mafic material. These studies may also reveal whether there are any unusual feldspathic KREEP-rich impact melt clasts in PCA 02007, like those reported in other lunar meteorites [15].

**Conclusions and Outlook:** PCA 02007 is a feldspathic regolith breccia with numerous impact melt and granulite clasts. These clasts are derived mainly from feldspathic highlands rocks, with exotic components from mare basalt and Mg-suite lithologies.

More than one impact event contributed to the formation of this rock, because its components were formed in different impact settings and were derived from at least three different types of parent rock. However, the number of impact events recorded in PCA 02007 is not possible to determine from available data. This number may be constrained by future Ar-Ar dating of the impact melt rock clasts, which will also provide information about the impact flux in regions of the Moon not sampled by the Apollo and Luna missions.

**References:** [1] Korotev R. L. et al. (2006) *Geochim. Cosmochim. Acta* 70, 5935–5956. [2] Zeigler R. A. et al. (2004) *LPS XXXV*, Abstract #1978. [3] Day J. M. D. et al. (2006) *Geochim. Cosmochim. Acta* 70, 5957–5989. [4] Joy K. H. et al. (2006) *LPS XXXVII*, Abstract #1274. [5] Taylor L. A. et al. (2004) *LPS XXXV*, Abstract # 1755. [6] Rasband W. S. ImageJ, National Institutes of Health, <http://rsb.info.nih.gov/ij/>. [7] Stöffler et al. (1980) *Proc. Conf. Lunar Highlands Crust*, 51-70. [8] Papike J. J. et al. (1991) *Lunar Sourcebook*, 121-181. [9] Jolliff B. L. et al. (1998) *Int. Geo. Rev.* 40, 916-935. [10] Korotev R. L. et al. (1994). *Geochim. Cosmochim. Acta* 58, 3931-3969. [11] Wiczorek M. A. et al. (2006) *Rev. Min. Geochem.* 60, 221-364. [12] Taylor G. J. et al. (1991) *Lunar Sourcebook*, 183-284. [13] Treiman A.H. et al. (2010) *Met. Planet. Sci.* 45, 163-180. [14] Stöffler D. et al. (2006) *Rev. Min. Geochem.* 60, 519-596. [15] Joy K. H. et al. (2010). *Met. Planet. Sci.* (In press).

**Acknowledgments:** I would like to thank the Meteorite Working Group, ANSMET, and their sponsors for providing a sample of PCA 02007 for this study; Georg Ann Robinson, Anne Peslier & D. Kent Ross (NASA-JSC) for their support with the instrumentation at JSC; Allan Treiman for providing an additional thin section of PCA 02007; and the LPI and Paul Spudis for organizing the summer intern program.

Table 1. Bulk composition (wt. % oxides) of PCA 02007. Totals for this study normalized to 100 wt. %.

	SiO <sub>2</sub>	Al <sub>2</sub> O <sub>3</sub>	TiO <sub>2</sub>	Cr <sub>2</sub> O <sub>3</sub>	FeO	MnO	MgO	CaO	NiO	Na <sub>2</sub> O	P <sub>2</sub> O <sub>5</sub>	K <sub>2</sub> O	Total
This study	44.14	26.46	0.31	0.13	6.57	0.06	6.08	15.74	0.10	0.35	0.03	0.04	100
<i>St. dev.</i>	<i>1.07</i>	<i>3.80</i>	<i>0.17</i>	<i>0.17</i>	<i>2.98</i>	<i>0.07</i>	<i>2.61</i>	<i>1.94</i>	<i>0.05</i>	<i>0.12</i>	<i>0.04</i>	<i>0.04</i>	
Joy et al. [4, 15]	43.41	25.71	0.28	0.171	6.3	0.09	6.8	15.19	0.05	0.36	0.03	0.03	98.42
Day et al. [3]	38.6	29.06	0.28	0.17	6.8	0.09	7.4	17.26	0.04	0.38	0.08	0.05	100.21
Korotev et al. [1]	44.80	26.50	0.29	0.16	6.26	0.09	6.70	15.40	0.05	0.33	0.03	0.02	100.60

## New insights into the structure and evolution of large volcanoes on Venus from high-resolution stereo-derived topography.

K. R. Verner<sup>1</sup>, G. A. Galgana<sup>2</sup> and P. J. McGovern<sup>2</sup>  
<sup>1</sup>Huffington Department of Earth Sciences, Southern Methodist University, Dallas, TX 75275, USA (kverner@smu.edu), <sup>2</sup>Lunar and Planetary Institute, 3600 Bay Area Blvd., Houston, TX, 77058, USA (galgana@lpi.usra.edu, mcgovern@lpi.usra.edu).

**Introduction:** The Magellan spacecraft mission to Venus during the 1990s provided 98% global coverage of synthetic aperture radar (SAR) imagery and nadir-looking altimeter data. Over 150 gently-sloping volcanic edifices with an average diameter of >100 km were identified [1,2]. The study of these volcanoes has been hampered by lack of high-resolution topography data, which only has a 10-20 km horizontal resolution. This is sufficient in capturing broad-scale shapes of edifices, but moderate- to small-scale tectonic features, such as summit calderae, radiating pit-chains and graben systems, are poorly or not at all resolved. These smaller surface features offer important constraints on volcanic processes, including sub-surface storage, movement of magma, and lithospheric flexure on the state of stress in the edifice [3, 4]. We impose a study of surface strain to understand these volcanic processes. Determining the amount of strain a surface has undergone is an important measurement for discriminating between different possible processes occurring in the interior of Venus.

**Data:** Until now, computational constraints hindered scientists' more detailed study of this dataset which would allow creation of topography via radargrammetry. The Magellan mission employed this method of obtaining topography through a cycle of repeat pass imaging, covering an area roughly within 40°N-40°S latitude and 60°E-180°E longitude. Scientists at the University of Alaska Fairbanks generated the digital elevation models used in this study, providing 1-3 km horizontal resolution [5, 6]. More than 30 large volcanic edifices are found in this region; several of these can be structurally analyzed because of their extensive systems of extensional radial faulting. These radial faults, as well as flank eruptive sites give hints to the origin and modes of magma ascent and emplacement [7].

In this research, we selected seven volcanic systems that exhibit a sufficient number of radial and circumferential faults. These volcanic systems

include four large volcanoes (Kunapipi Mons, Anala Mons, Irnini Mons and Gula Mons), and four large radiating fracture systems (RFCs such as Didilia Mons, Pavlova Corona, and H'uraru Corona). Measurements were taken on the merged GTDR and stereo DEM datasets, along with the raw and filtered versions of each DEM.

**Methods:** We used the image processing software ENVI to create 3D visualizations of volcanic features, combining the left-view backscatter images with the stereo DEMs. This helped us determine which faults and fractures have sufficient offsets that would be useful for structural interpretation. Ideally, volcanoes with more than two resolvable radiating fractures were utilized in this study. To provide accurate measurements, strike-trending profiles were taken along identified faults and fractures, supplemented by perpendicular cross-sections. Topographic profiles based on the high-pass filtered digital elevation models (DEM\_H) were used in measuring the throw of faults and fractures. Following [8], extension was determined by:

$$\Delta W = \frac{d}{\tan \theta}$$

where  $\Delta W$  is the minimum amount of extension,  $d$  is the depth of the fault and  $\theta$  is the fault dip angle (taken to be 60° to represent the original fault surface strain for a normal fault). The hoop strain was calculated by summing the extension measurements and dividing by the circumference around the RFC:

$$\varepsilon(r) = \frac{\sum \Delta W(r)}{2\pi r}$$

where  $r$  is the radius from center. These measurements could then be used as quantitative constraints to identify volcano-tectonic processes that have contributed to edifice development. We then use MATLAB codes that compute radial and

vertical strains due to an inflating spherical magmatic source [9] and compare the results with actual strain measurements.

**Results:** We note significant improvement in the interpretability of structural features in the images, as the combined display of topography and backscatter images enabled precise measurement of fracture openings and fault offsets in three dimensions. In particular, the improved DEM of Kunapipi Mons and Anala Mons give new perspectives on the nature of flank-trending faults and how these are related to the structural development of these volcanoes (Figures 1 and 2). In the case of Kunapipi Mons, the area near the summit was traversed by a NE-SW and NW-SE trending fracture system. These indicate the large strains undergone by the volcanic edifice possibly due to magmatic inflation and/or uplift (Figure 1). In the case of Anala Mons, the NNE-SSW trending, summit-crossing fracture system show considerable fault throws that indicate large deformation events undergone by the edifice during its development (Figures 2 and 3).

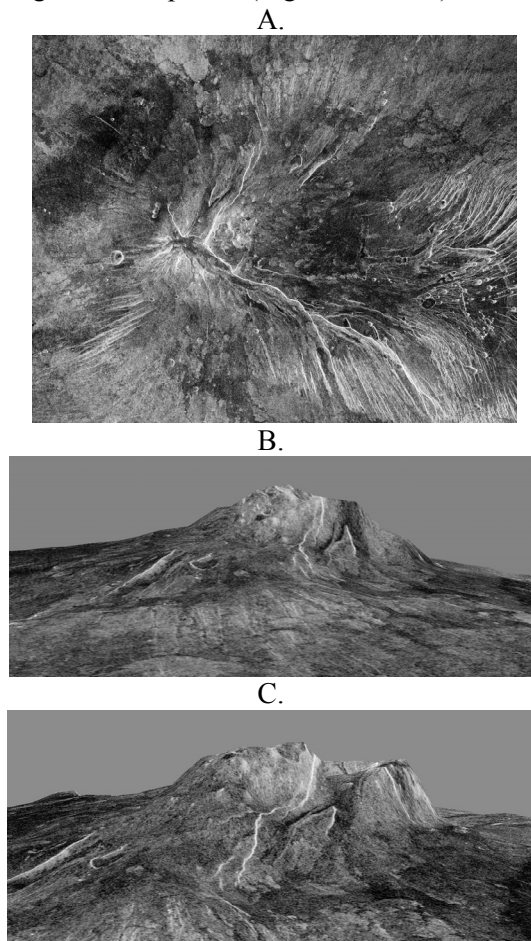


**Figure 1 (Left, below).** (A) Magellan left-viewing backscatter image of Kunapipi Mons, showing extensive radiating fractures and lava flows; (B): Radar backscatter image draped on GTDR dataset, showing Kunapipi Mons summit, in perspective view (view towards the south). Vertical exaggeration (VE) = 30x ; and (C): Radar backscatter image of Kunapipi Mons draped over stereo dataset in perspective view (view towards south), revealing summit depression produced by radiating fracture, VE = 30x.

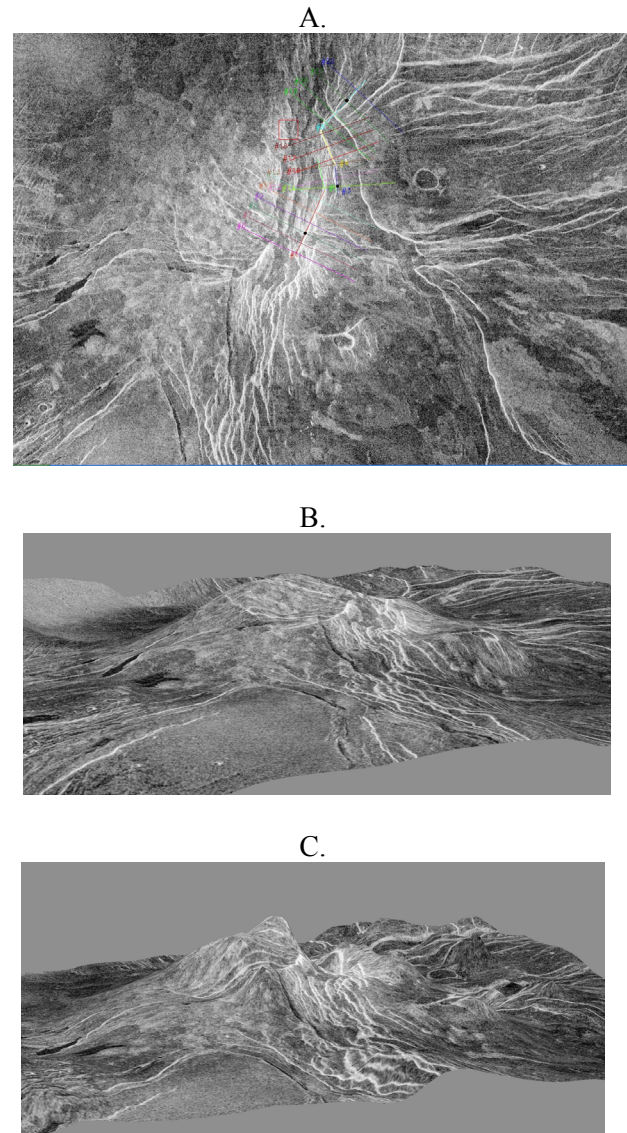


**Figure 2:** (A) Left-viewing Magellan back-scatter image of Anala Mons, showing extensive radiating fractures through its summit; (B): Radar backscatter image draped on GTDR dataset, showing Anala Mons summit, in perspective view (view towards the northeast). Vertical exaggeration (VE) = 20x ; and (C): Radar backscatter image of Anala Mons draped over stereo dataset in perspective view (view towards northeast), revealing summit depression produced by rift-like fracture, VE = 20x.

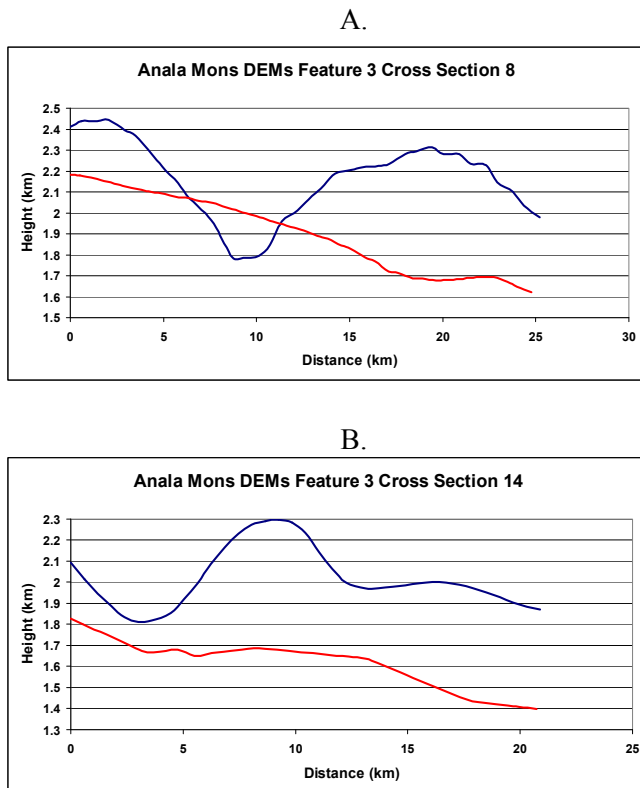


**Figure 3.** Near-summit topographic cross-sections for (A) Cross-section 8 from feature 3 on Ana Mons and (B) Cross-section 14 from feature 3 on Ana Mons. Blue line shows stereo topography (DEM\_H) and red line shows GTDR topography. An arbitrary vertical offset of ~200 m separates the two datasets for visibility. Profiles show significant improvement in the resolved topography, allowing the measurement of fault offsets.

**Discussion.** Increased resolution of topographic features found on volcanic edifices improves our structural interpretation significantly. This affects the modeling process, and enables new techniques to quantify volcano deformation and trace the origin and pathways of magma. Our preliminary inversion results resolve the location of spherical magmatic sources underneath the edifices. These help the modeling effort to initially locate the centers of magmatic inflation or deflation, and constrain the depth and volumetric changes.

Numerical models of large volcano deformation predict that hoop and radial strains gradually diminish as a function of distance from the inflationary source. Our results generally do not show a strong trend of this nature. Our measured strain values were observed to be incongruent in magnitude compared to that expected from radial diking. Compared to [8] our strain measurements

are an order of magnitude smaller and show no common trend (i.e. strain measurement values show ambiguous patterns along the fault profile).

Radial and hoop strains inferred from models show unrealistically high values that are highly variable along the radius. A possible explanation is that intrusions that directly ascend from the mantle contribute an extra component of extension at higher radial distances. Furthermore, these patterns also suggest that such fault offsets are probably not caused by a single, centralized inflationary event, but perhaps by a series of intrusive magmatic events, or tainted by tectonic and other volcanic processes such as rifting and magma-induced dike propagation [10].

**Future work.** In future processing activities, we plan to investigate similar volcanic structures and incorporate inversion techniques that utilize different source geometries to better constrain magmatic source locations and deformation patterns. In addition, we plan to investigate the effects contributed by a flexing lithosphere in the faulting process. These models, in combination with high resolution topographic data from our stereo-derived datasets, will significantly advance the understanding of how volcanic edifices deform and how magma ascends through subsurface intrusions.

**Acknowledgments:** We are grateful to Dr. Robert Herrick (Univ. Alaska-Fairbanks) for providing the Magellan stereo DEMs used in this research.

## References:

- [1] Head et al. (1992), *JGR*, 97(E8): 13,153-13,197.
- [2] Crumpler, L. et al. (1997), In Bougher et al., *Venus II*, pp. 697-754.
- [3] Grosfils E. and J. Head (1994), *GRL*, 21(8):701-704.
- [4] McGovern P. and S. Solomon (1998), *JGR*, 103:11, 071-11,101.
- [5] Gleason, A. et al. (2010). *JGR*, 115, E06004, doi:10.1029/2009JE003431.
- [6] Herrick, R. et al. (2010), *LPSC*, Abstract 1622.
- [7] Janes, D. and S. Squyres (1993), *GRL*, 20(24): 2,961-2,964.
- [8] Grindrod, P. et al. (2005), *JGR*, 110, E12002, doi:10.1029/2005JE002416.
- [9] McTigue, D. (1987). *JGR*, 92(B12): 12,931-12,940.
- [10] Rubin, A. (1995), *Annu. Rev. Earth Planet. Sci.*, 23 :287-336.

**COVARIANT C AND O ISOTOPE TRENDS IN SOME TERRESTRIAL CARBONATES AND ALH 84001: POSSIBLE LINKAGE THROUGH SIMILAR FORMATION PROCESSES.** Kathryn E. Volk<sup>1</sup>, Paul B. Niles<sup>2</sup>, Richard A. Socki<sup>2,3</sup>, <sup>1</sup>Northern Illinois University Department of Geology and Environmental Geosciences, DeKalb, IL 60115 (kvolk@niu.edu), <sup>2</sup>NASA–Johnson Space Center, Houston, TX 77058, <sup>3</sup>ESCG, (paul.b.niles@nasa.gov, richard.a.socki@nasa.gov)

**Introduction:** Carbonate minerals found on the surface of Mars and in martian meteorites indicate that liquid water has played a significant role in the planet's history [1-5]. These findings have raised questions regarding the history of the martian hydrosphere and atmosphere as well as the possibility of life. Of particular interest are the 3.9 Ga carbonates found in the ancient martian meteorite ALH 84001 [6,7]. Ancient Mars may have resembled the extreme environments we see today where any liquid water only exists in brief aqueous events and is subject to fast freezing and/or high evaporation [3,8]. Considering the current inaccessibility to Mars, terrestrial analogs are valuable tools for understanding formation mechanisms of carbonates in martian meteorite ALH 84001. To find suitable analogs we must look for environments on earth where water is subject to similar extremes as what might be found on Mars.

Carbonates in ALH 84001 exhibit a covariant isotope trend:  $\delta^{18}\text{O}$  values range from -10 to +25‰ (VSMOW) and  $\delta^{13}\text{C}$  range from +30‰ to +64‰ (VPDB) [4,7,9,10]. A covariant trend is also observed in bulk samples of terrestrial carbonates from Sunset Crater, Arizona, USA and Ellesmere Island, High Arctic, Canada. Knauth et al. [9] analyzed carbonate crusts from Sunset Crater and found covariant isotope trends in subaerial carbonates. Blake [11] analyzed a number of carbonate samples from Ellesmere Island and recorded enriched  $\delta^{13}\text{C}$  values that correlated with higher  $\delta^{18}\text{O}$  values.

Environmental conditions at Sunset crater, Arizona and Ellesmere Island, Canada resemble those found on Mars [7,8,9], making them prime candidates for analog research.

We hypothesize that covariant  $\delta^{13}\text{C}$  and  $\delta^{18}\text{O}$  trends in Sunset Crater and Ellesmere Island carbonates are related to covariant  $\delta^{13}\text{C}$  and  $\delta^{18}\text{O}$  trends in ALH 84001 carbonates by similar formation mechanisms. In this study we seek to identify discrete micro-scale isotopic variation within the carbonate crusts to understand their formation mechanisms and by doing so gain insight into carbonate formation of ALH 84001.

**Methods:** Three Sunset Crater samples were analyzed from subaerial basalt pinnacles on a lava flow near Sunset Crater, Arizona (4, 8, and 10). The carbonates grew attached to the underside of basalt pinnacles and were never exposed to the soil [9]. Chunks of basalt with carbonate coating were broken from the rock

and mounted in epoxy. The epoxy was then cut with an Isomet lapping saw into thick sections providing slices of rock with a basaltic interior and a carbonate ring around the edge 100 to 350  $\mu\text{m}$  wide (Fig. 1). Carbonate material was removed from the thick sections using a NewWave Technology Micromill. The carbonate rims were drilled 1 to 7 times at separate points from a single crust and 300  $\mu\text{g} \pm 100\mu\text{g}$  of sample was collected each time.

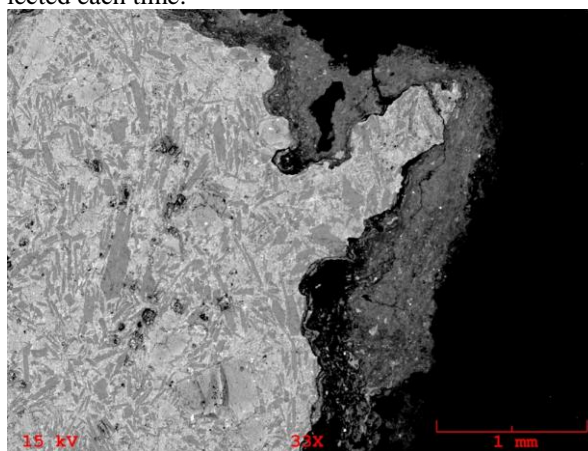


Figure 1. SEM Backscatter image of Sunset Crater rock. The carbonate appears as darker material around the basaltic interior.

Three Ellesmere Island samples from two individual crusts (28-1, 28-3, and 260-3) were analyzed in a similar manner to Sunset Crater carbonates. Ellesmere Island carbonates were supplied to us from Wes Blake of the Canadian Geological Survey. These crusts were 1 to 2 cm long and prepared as thick sections exposing cross sections of their growth layering. Using the Micromill  $\sim 200 \times \sim 2000 \mu\text{m}$  area of powdered carbonate sample approximately 100  $\mu\text{g} \pm 50 \mu\text{g}$  was removed from the carbonate sample sections along growth patterns. Each section yielded 10 to 15 milled swaths.

Backscatter images were obtained from samples at 15kV and 50x using the 5910LV JEOL SEM at Johnson Space Center. EDS was conducted on select spots of some samples. This demonstrated that the chemical composition of the Sunset Crater and Ellesmere Island samples are  $\text{CaCO}_3$ . The powdered carbonate samples were reacted with 100% phosphoric acid at 72°C and analyzed for carbon and oxygen isotope composition via Thermo Gas Bench II/MAT 253 IRMS system operating in continuous flow mode.

The data was corrected using 2 standards: NBS-18, and NBS-19. The uncertainties are reported in  $2\sigma$ . The uncertainty includes reproducibility of the standards, standard deviation within each analysis, and reproducibility of reference gas injections. The reproducibility of standards was our largest source of error at 0.3 for  $\delta^{13}\text{C}$  and 0.2 for  $\delta^{18}\text{O}$ .

**Results:** We report a  $\delta^{13}\text{C}$  range of +1.8 to +12.7‰, and a  $\delta^{18}\text{O}$  range of +21.5 to +29.0‰ for Sunset Crater samples. There is a significant enrichment in  $^{13}\text{C}$  compared to most terrestrial carbonates. Our method of microdrilling removed discrete micro-samples rather than the average bulk sample as had been done in previous studies [8]. This demonstrated heterogeneity within the crust and identified covariant trends from each individual sample that were not as visible from previous sampling methods. The trend is true for whole areas 4, 8, and 10 (Fig 2), as well individual crusts (Fig 3).

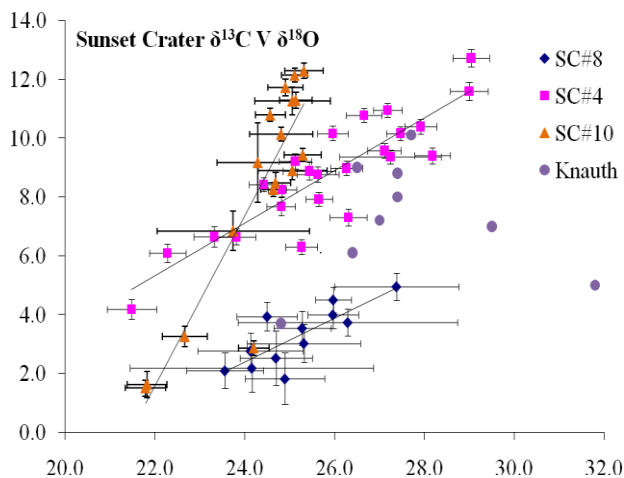


Figure 2. All data (4, 8, 10) from Sunset Crater, Arizona plus previous data by Knauth [9]. Our data shows a distinct and persistent covariant enrichment trend.

The Ellesmere Island samples also displayed an unusually heavy range of  $\delta^{13}\text{C}$  values of +3.0 to +12.2‰. But they exhibited less variation in  $\delta^{18}\text{O}$  isotopes: +15.4 to +17.6‰. Samples 28-1 and 28-3 showed a covariant trend, while sample 260-3 did not. In each sample there was a general enrichment pattern across the sample. For example in 28-3 the heaviest isotopes were on the outside of the crust and the lightest isotopes were on the inside.

**Discussion:** The two most likely explanations for the  $^{13}\text{C}$  enrichment observed in both of our sampling locations are:  $\text{CO}_2$  degassing or photosynthesis. During evaporation  $\text{CO}_2$  is concentrated and degassing results [12].  $\text{CO}_2$  degassing can also happen if the  $P_{\text{CO}_2}$  of the

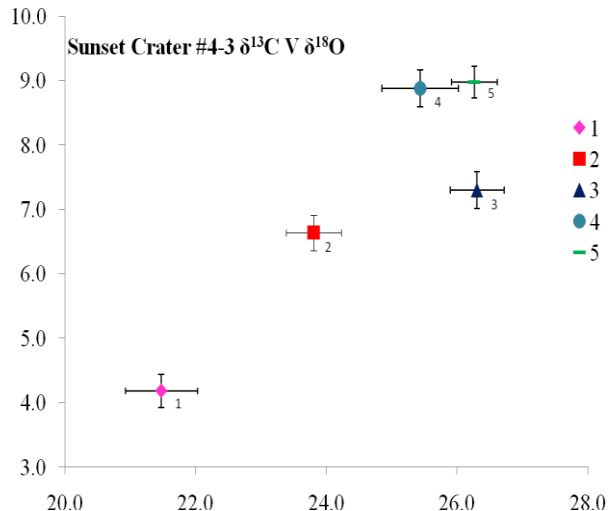


Figure 3. This data from one particular crust (crust 4-3) shows a progressive covariant enrichment from one discrete sampling point to another, and significant micro-scale heterogeneity.

$\text{HCO}_3^-$  solution is significantly different from the atmosphere. This is most common in cave environments when water, percolating through the soil environment, has a high  $P_{\text{CO}_2}$  and enters the cave environment where the  $P_{\text{CO}_2}$  is much lower [12-15]. This process can also result in simultaneous smaller enrichment of  $^{18}\text{O}$  as demonstrated by Mickler et. al.[15]. If precipitation of carbonate during  $\text{CO}_2$  degassing is faster than  $\text{CO}_2$  hydration and hydroxylation reactions then the oxygen in the  $\text{HCO}_3^-$  is unable to re-equilibrate with the water [15]. The result is a positive covariant isotope enrichment trend. If however precipitation of carbonate is slow, then bicarbonate oxygen is able to re-equilibrate with the water and there is no enrichment in O while C is enriched [15]. Clark and Lauriol [16] demonstrated rapid freezing also induces  $\text{CO}_2$  degassing and that this process leads to a simultaneous enrichment of  $^{18}\text{O}$  and  $^{13}\text{C}$ . Alternatively, photosynthesis is a biologic process that leads to  $^{13}\text{C}$  enrichment in carbonates due to the preferential removal of light  $\text{CO}_2$  during the photosynthetic process [9,12, 16]. As mentioned  $\text{CO}_2$  degassing can enrich both  $^{13}\text{C}$  and  $^{18}\text{O}$ , but photosynthesis will only alter C isotopes.

The O isotopes are also affected by evaporation which preferentially removes  $^{16}\text{O}$ -rich water enriching precipitated carbonate in  $^{18}\text{O}$ . Evaporation, by shrinking the solution and concentrating the  $\text{CO}_2$ , can result in a simultaneous enrichment of both isotopes [12].

Knauth et al. [9] analyzed bulk carbonates from Sunset Crater and argued that degassing is unlikely on the basalt pinnacles due to the lack of sufficient  $\text{CO}_2$  in

the fluids; therefore he stated that photosynthesis is the most likely mechanism for  $^{13}\text{C}$  enrichment trends. However our sampling method of the Sunset Crater data captured more defined covariant trends showing strong linkage between O and C isotopic composition. Leveille et. al. [12] studied carbonates enriched by photosynthesis and evaporation in Hawaiian caves and found no significant correlation in isotope trends. The isotope trend in all three locations we sampled and in individual crusts at each location is more consistent with enrichment due to a combination of evaporation and degassing because of the close covariance of O and C in each sample. An understanding of the evaporation rate,  $P_{\text{CO}_2}$  of  $\text{HCO}_3^-$  solution, and  $\delta^{13}\text{C}$  values of coexisting organic matter at Sunset Crater may be useful in future research. A possible experiment that may provide a way to discern biologically induced enrichment versus abiotic would be to model Sunset Crater carbonate formation in the absence of photosynthetic organisms and analyze the isotope effects.

The Ellesmere Island samples are from colder periods of the Holocene and are thought to have formed under thin, stationary, carapace ice caps [11]. Carbon age dating place sample 28-1 and 28-3 between 2000 and 3000 years old while sample 260-3 is 5000 years old [11]. The samples are enriched in  $^{13}\text{C}$ , while  $^{18}\text{O}$  shows small variation. Due to the role of ice, cryogenic  $\text{CO}_2$  degassing as described by Clark and Lauriol [16] may be the best explanation for the positive covariant isotope trend observed in 28-1 and 28-3. Sample 260-3 did not display a covariant trend, instead showing  $^{13}\text{C}$  enrichment with no variation in  $^{18}\text{O}$ . Photosynthesis may be an explanation for this enrichment pattern since it would only affect the carbon [11]. This type of enrichment pattern can also be produced abiotically during slower  $\text{CO}_2$  degassing allowing oxygen to equilibrate [15]. An experiment that allows carbonate to precipitate via kinetics versus photosynthesis under cryogenic conditions may shed light onto isotope effects of these two processes.

The isotope enrichment ranges in ALH 84001 carbonates are significantly more extensive than isotope ranges in the terrestrial analogs: ~30‰ for  $\delta^{13}\text{C}$  and ~30‰ for  $\delta^{18}\text{O}$  [2,5,8,9]. Despite this, the positive covariant trend in Sunset Crater is similar to that observed in ALH 84001. The similarity of these isotope trends suggests that Sunset Crater carbonates and ALH 84001 carbonates formation are most similar. Thus it seems reasonable that ALH 84001 enrichment trends may be a result of evaporation and  $\text{CO}_2$  degassing operating under more extreme circumstances. While a photosynthetic process cannot be ruled out, the covariant trend suggests that the enrichment mechanisms are linked through coupled processes rather than

chance. Sunset Crater is a dry environment with relatively high evaporation and brief periods of precipitation. This type of environment has also been hypothesized for Mars [7]. Sunset Crater then may provide the best analog example of the ancient martian environment and carbonate formation processes and should be examined in more detail.

**Conclusion:** In this study we found large covariant micro-scale variations of C and O isotopes of the terrestrial carbonates, particularly with Sunset Crater. The Sunset Crater carbonates represent a smaller magnitude version of ALH 84001 carbonates. The positive covariant enrichment trend observed in Sunset Crater is most likely a result of evaporation and abiotic  $\text{CO}_2$  degassing. Thus these same mechanisms may also be responsible for ALH 84001 carbonates although with greater magnitude. Sunset Crater's similarity to ALH 84001 carbonates makes it a good candidate for explaining martian carbonates and a more thorough study of their formation is pertinent to understanding the formation of ALH 84001 carbonates.

**Acknowledgement:** I would like to thank the Lunar and Planetary Institute for providing this research opportunity.

**References:** 1. Carr, M., *Water on Mars*, Oxford University Press, New York, (1996). 2. Head, J., et. al., *LPSC XXX*, Abs. No. 1352. 3. Kieffer, H.H., et. al., *Mars*, University of Arizona Press, Tucson, (1992). 4. McSween, H.Y., *Meteoritics*, **29**, 6, 757-779 (1994). 5. Socki, R.A., et. al. *LPSC XXXVI* Abs. No. 1703 (2005). 6. Borge, L.E., et. al., *Science*, **286**, 5437, 90-94 (1999). 7. Niles, P.B., et al., *Geochim. Cosmochim. Acta*, **69**, 2931-2944 (2005). 8. Socki, R.A., et. al., *LPSC XXXX*, Abs. No. 2218 (2009). 9. Knauth, L.P., et al., *Geochim. Cosmochim. Acta* **67**, 185-195 (2002). 10. Romanek, C.S., et. al., *Nature*, **372**, 655-657 (1994). 11. Blake, W., *Geografiska Annaler Series a-Physical Geography* **87A**, 175-192 (2005). 12. Leveille, R.J., et. al. *Geobiology*. **5**, 235-249 (2007). 13. Hendy, C.H., *geochim. Chosmonchim. Acta*, **35**, 801-824 (1971), 14. Holland, H.D., et. al., *The Journal of Geol.* **72**, 1, 36-67 (1964). 15. Mickler, P.J., et al., *GSA Bulletin* **118**, 65-81 (2006). 16. Clark, and B., Lauriol, *Chem. Geol.* **102**, 217-228 (1992). 17. Werner, S., Morgan, J.J, *Aquatic Chemistry*, John Wiley & Sons, NY (1996).

**PHYLLOSILICATE DEPOSITS IN SHALBATANA VALLIS** Anne E. Wintzer<sup>1</sup>, Carlton C. Allen<sup>2</sup>, and Dorothy Z. Oehler<sup>2</sup>. <sup>1</sup>University of Arkansas (Center for Space and Planetary Sciences, 202 Old Museum Building, Fayetteville, Arkansas 72701, awintzer@uark.edu), <sup>2</sup>NASA Johnson Space Center, Astromaterials Research and Exploration Science (ARES) Directorate, 2101 NASA Parkway, Houston, TX 77058.

**Introduction:** Shalbatana Vallis is an ancient river valley on Mars, the westernmost of the southern Chryse outflow channels (Fig. 1). The geologic history of this area has significant implications for understanding Mars' hydrologic and climate history. The highland flood basalts are cut by large collapse depressions, multiple outflow channels, and chaotic terrain. An intravalley paleolake with a depth of over 400 m, in the 125 km diameter Orson Welles crater (Fig. 2) and the adjacent section of Shalbatana Vallis, was deduced from Mars Orbiter Laser Altimeter (MOLA) topography, evidence of shorelines and the occurrence of fan-delta deposits, including Gilbert-style deltas [1].

A number of CRISM (Compact Reconnaissance Imaging Spectrometer for Mars) images with strong phyllosilicate signatures have been identified throughout the channel and nearby highlands (Fig. 2). A majority of the signatures are concentrated in areas exposed by impact cratering. Since such minerals form by a variety of different geological processes, such as weathering, burial diagenesis, and hydrothermal alteration [2], the nature of the phyllosilicate deposits in the Shalbatana Vallis region can provide insights into the possible formation processes that took place and enable determination of constraints on the early aqueous activity in the region.

We contribute to the understanding of the geologic history of Shalbatana Vallis using data from the HiRISE (High Resolution Imaging Science Experiment) and CTX (Context) cameras and the CRISM spectrometer on the MRO (Mars Reconnaissance Orbiter) spacecraft, and evaluating the mineralogy, origin, and placement of Fe/Mg-rich and Al-rich phyllosilicates in the region.

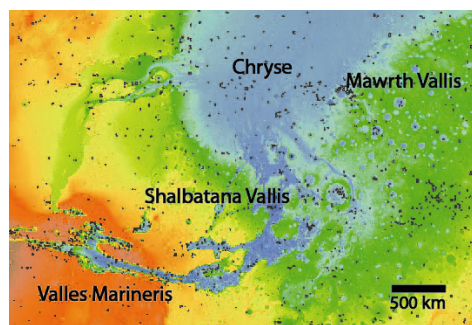


**Figure 1.** MOLA topographic map of the area surrounding Shalbatana Vallis. Dark spots are locations of CRISM footprints.

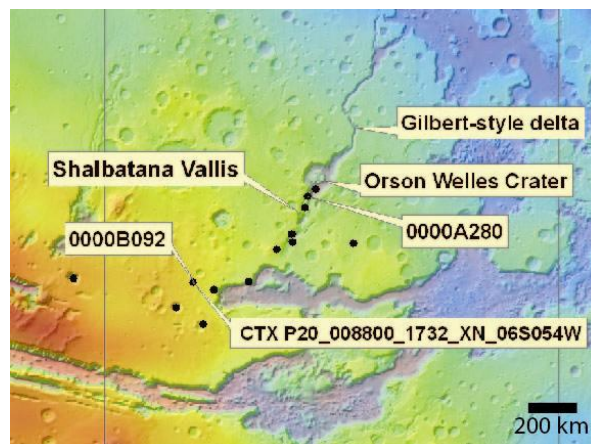


**Figure 2.** MOLA topographic map of Shalbatana Vallis, black dots indicating positions of CRISM images with strong phyllosilicate signatures.

**Methods:** Using the *ir\_phy* browse products found on the CRISM website, <http://crism.jhuapl.edu/>, areas were selected within Shalbatana and the surrounding highlands that display strong phyllosilicate signatures, either red for Fe/Mg-rich compositions or green for Al-rich compositions. These images were then overlain on HiRISE images of the same location in order to choose the best areas to extract spectra and determine in higher resolution the correlated geologic features (Fig. 3). Using standard techniques, atmospheric correction was performed on the raw CRISM images using CAT (CRISM Analysis Tool) in conjunction with ENVI Image Processing software. Using IR wavelengths, eight spectra were extracted from 5x5 pixel spots in the corrected image that displayed high concentrations of phyllosilicates. These spectra were then ratioed to spectrally unremarkable spots of equal size in the same column in order to reduce column-dependent instrumental artifacts and to clarify mineral features. All eight ratio spectra were then averaged. The averaged ratio spectra were then compared to standard laboratory spectra from the CRISM Spectral Library. Topographic data from HiRISE were used to aid in regional stratigraphic correlations and improve our understanding of the three-dimensional geometries of the phyllosilicate-rich layers.

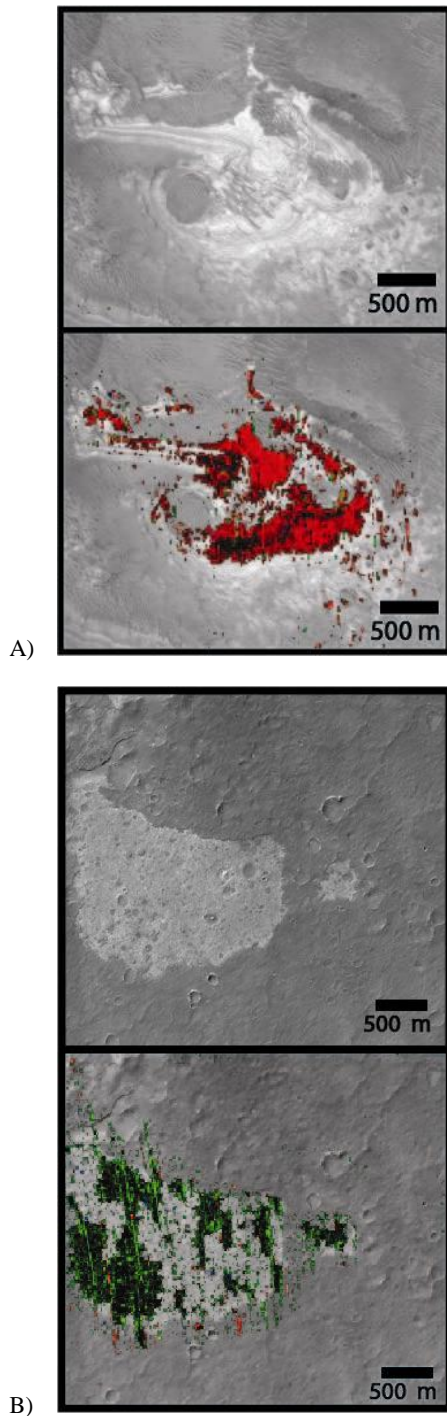


**Figure 3.** A) HiRISE image PSP\_007455\_1785 (on top); shown with ir\_phy overlay of CRISM 0000A280 (on bottom) B) HiRISE image PSP\_008800\_1730 (on top); shown with ir\_phy overlay of CRISM 0000B092

**Results:** A majority of the phyllosilicate-rich areas sampled were dominated by Fe/Mg compositions. These were all observed within the rims of craters or the valley walls. The Fe/Mg phyllosilicates exhibited absorption bands near 1.45  $\mu\text{m}$ , 1.9-1.95  $\mu\text{m}$ , and 2.25-

2.3  $\mu\text{m}$  consistent with nontronite  $((\text{CaO}_{0.5}, \text{Na})_{0.3} \text{Fe}^{3+}_2 (\text{Si}, \text{Al})_4 \text{O}_{10} (\text{OH})_2 \cdot n\text{H}_2\text{O})$ . The Fe/Mg-rich phyllosilicates were detected in continuous layers (Fig. 4) at altitudes ranging from 1939m in the highlands to -1261m in the upper portion of the valley. The Al-rich phyllosilicates were exposed in the highland plains, as well as near the deepest point in Orson Welles crater. Those in the highland plains are located within shallow angular depressions (Figs. 3B, 5). The Al-rich phyllosilicates exhibit bands near 1.5  $\mu\text{m}$  that are consistent with prehnite  $(\text{Ca}_2\text{Al}(\text{AlSi}_3\text{O}_{10})(\text{OH})_2)$  as well as bands at 1.44  $\mu\text{m}$  and 2.21  $\mu\text{m}$  consistent with kaolinite  $(\text{Al}_2\text{Si}_2\text{O}_5(\text{OH})_4)$  as well as montmorillonite  $((\text{Na}, \text{Ca})_{0.33}(\text{Al}, \text{Mg})_2(\text{Si}_4\text{O}_{10})(\text{OH})_2 \cdot n\text{H}_2\text{O})$  (Fig. 6). These exposures are most likely mixtures of several Al-rich clays. These findings are consistent with mineral compositions found previously by Carter *et al.* [2] in the northern plains.

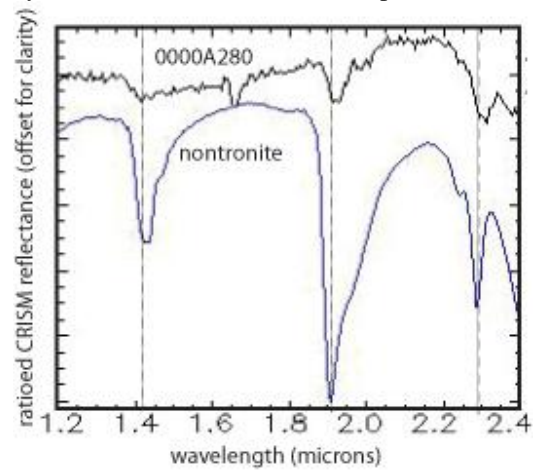


**Figure 4.** Ratioed spectrum of CRISM 0000A2880 compared with laboratory spectrum for nontronite; band at 1.66  $\mu\text{m}$  is instrument artifact

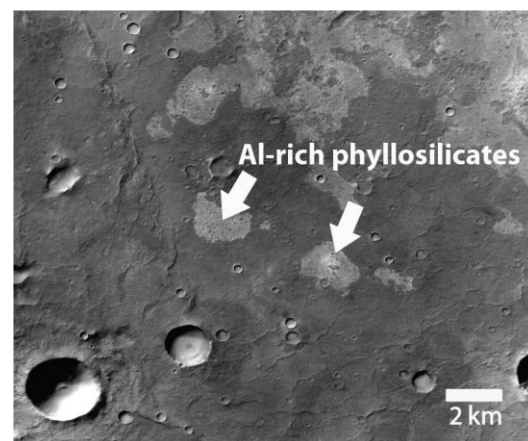


**Figure 5.** CTX image P20\_008800\_1732\_XN\_06S054W\_ showing shallow angular depressions containing Al-rich phyllosilicates; includes areas shown in 3B

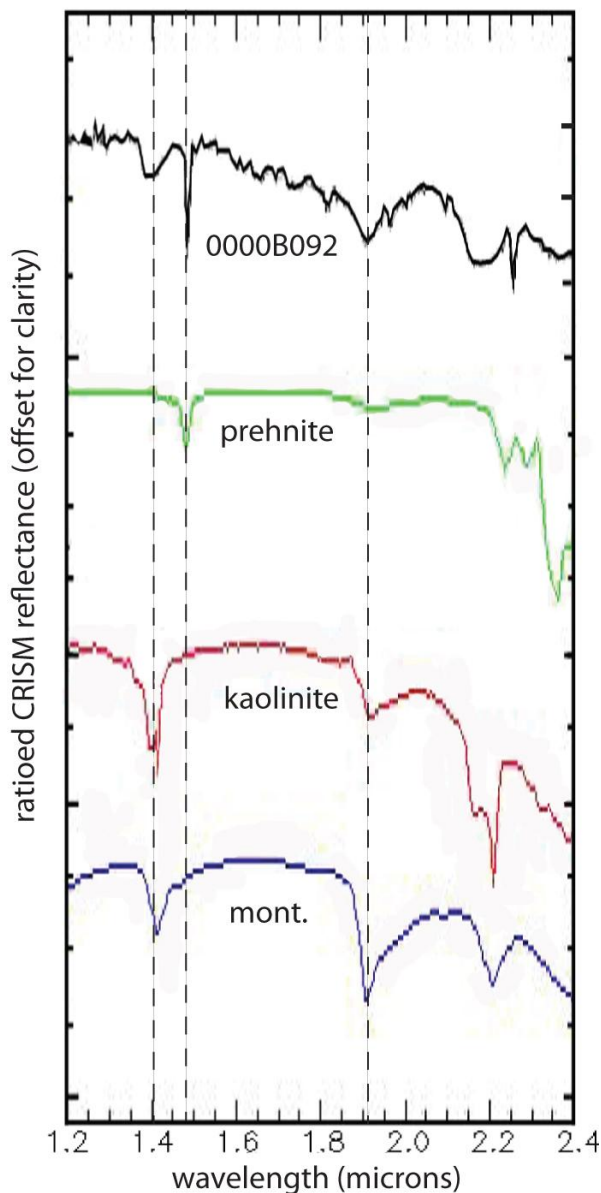


**Figure 6.** Ratioed spectrum of CRISM 0000B092 compared with laboratory spectra of prehnite, kaolinite, and montmorillonite

**Discussion:** All exposures of Fe/Mg-rich phyllosilicates are distinctly layered (Fig. 3A) and occur at various altitudes throughout the highlands and channel area, analogous to multiple phyllosilicate-rich interbeds within layers of flood basalts. Nontronites are also typical alteration products of basalts [3] and current data are not sufficient to differentiate between a detrital and an authigenic origin. No Fe/Mg-rich signatures were found in the valley north of Orson Welles crater, nor in the adjacent Chryse lowlands, indicating that any sink deposit was either not visible due to dust covering, was removed by erosion, or is in a location not yet covered by CRISM.

There are fewer examples of Al-rich phyllosilicates in the region, and the signatures are found in both the highlands and deep within Orson Welles crater. These phyllosilicates could either be products of aqueous alteration and leaching of Fe and Mg from the highland rocks or alteration of a later Si-rich volcanic ash or sediment [4]. The Al-rich phyllosilicates within the highlands appear to be remnants of a continuous stratigraphic layer and possible source deposit for the Al-rich phyllosilicates seen at a lower elevation within Orson Welles crater. The angular shape of the depressions containing the Al-rich deposits in the highlands (Fig. 4) may also be an erosional feature related to the desiccated texture seen on the surface. The Al-rich phyllosilicates within the basin of Orson Welles are scattered and display no clear layering. This would suggest that these are sediments transported during a flood event or deposited in the crater lake. This is the only location within the study area where geologic relationships favor detrital phyllosilicates.

**Future Work:** Continued spectral analysis of phyllosilicates is needed to correlate continuous layers of sediment across the region. The area north into Chryse and Acidalia also needs to be studied further to determine if there are identifiable sinks for the phyllosilicates. There is limited CRISM data in the area so as more images are collected from the spacecraft, further interpretation will be possible.

**Acknowledgements:** I would like to thank the Lunar and Planetary Institute and the JSC ARES Directorate for this opportunity and their support of this research.

**References:** [1] Di Achille, G. *et al.* (2009) *Geophys. Res. Lett.*, **36**, L14201, doi:10.1029/2009GL038854. [2] Carter, J. *et al.* (2010) *Science*, **328**, 1682-1686. [3] Velde, B., ed. (1995) *Origin and Mineralogy of Clays*, Springer-Verlag. [4] Bishop J. L. *et al.* (2008) *Science*, **321**, 830-833.

## NOTES

---